

Article

Mineralogy and Geochemistry of the Paleocene–Eocene Palana Formation in Western Rajasthan, India: Insights for Sedimentary Paleoenvironmental Conditions and Volcanic Activity

Mohammed Hail Hakimi ^{1,*}, Alok Kumar ², Abdullah M. Alqubalee ³, Alok K. Singh ⁴, Mohammed Almobarky ⁵, Afikah Rahim ⁶, Mohammad Alqudah ⁷, Aref Lashin ⁵, Khairul Azlan Mustapha ² and Waqas Naseem ⁸

¹ Department of Petroleum Engineering, Kazan Federal University, Kazan 420008, Russia

² Department of Geology, University of Malaya, Kuala Lumpur 50603, Malaysia

³ Center for Integrative Petroleum Research, College of Petroleum Engineering and Geosciences, King Fahd University of Petroleum and Minerals, Dhahran 31261, Saudi Arabia

⁴ Rajiv Gandhi Institute of Petroleum Technology, Jais 229304, India

⁵ Petroleum and Natural Gas Engineering Department, College of Engineering, King Saud University, Riyadh 11421, Saudi Arabia

⁶ Department of Geotechnics & Transportation, Faculty of Civil Engineering, Universiti Teknologi Malaysia, Johor Bahru 81310, Malaysia

⁷ Department of Earth and Environmental Sciences, Yarmouk University, Irbid 21163, Jordan

⁸ Department of Geology, University of Poonch Rawalakot, Azad Jammu & Kashmir, Rawalakot 12350, Pakistan

* Correspondence: ibnalhakimi@taiz.edu.ye



Citation: Hakimi, M.H.; Kumar, A.; Alqubalee, A.M.; Singh, A.K.; Almobarky, M.; Rahim, A.; Alqudah, M.; Lashin, A.; Mustapha, K.A.; Naseem, W. Mineralogy and Geochemistry of the Paleocene–Eocene Palana Formation in Western Rajasthan, India: Insights for Sedimentary Paleoenvironmental Conditions and Volcanic Activity. *Minerals* **2024**, *14*, 126. <https://doi.org/10.3390/min14020126>

Academic Editors: Jingchun Tian and Stephen E Laubach

Received: 22 November 2023

Revised: 13 January 2024

Accepted: 18 January 2024

Published: 24 January 2024



Copyright: © 2024 by the authors. Licensee MDPI, Basel, Switzerland. This article is an open access article distributed under the terms and conditions of the Creative Commons Attribution (CC BY) license (<https://creativecommons.org/licenses/by/4.0/>).

Abstract: Organic-rich shale rocks from the Paleocene–Eocene Palana Formation in western Rajasthan, India, were systematically investigated based on inorganic and organic geochemistry combined with microscopic examinations to evaluate the sedimentary paleoenvironmental conditions and volcanic activity and their impact on the high organic carbon accumulation. The Palana shales are categorized by high organic matter (OM) and sulfur contents, with total values up to 36.23 wt.% and 2.24 wt.%, respectively. The richness of phytoplankton algae (i.e., telalginite and lamalginite) together with redox-sensitive trace elements further suggests a marine setting and anoxic environmental conditions during the Paleocene–Eocene. The significant low oxygen conditions may contribute to enhancing the preservation of organic matter during deposition. The mineralogical and inorganic geochemical indicators demonstrate that the Palana organic-rich shale facies was accumulated in a warm and humid climate with moderate salinity stratification conditions in the water columns, thereby contributing to the high bioproductivity of the phytoplankton algae blooms within the photic zone. The presence of significant contents of zeolite derived from volcanic material together with silica minerals such as apophyllite and tridymite in most of the Palana organic-rich shales indicates a volcanic origin and supports hydrothermal activities during the Paleocene–Eocene period. These volcanic activities in this case are considered the influx of large masses of nutrients into the photic zone due to the ash accumulation, as indicated by the presence of the zeolites in the Palana shales. Therefore, the high bio-productivity associated with effective OM preservation led to the organic carbon accumulation in the Palana Formation during the Paleocene–Eocene.

Keywords: organic-rich shale; bioproductivity; anoxia conditions; organic accumulation; Rajasthan; western India

1. Introduction

Black shale sedimentary rocks, commonly referred to as organic-rich mudstone and oil shale, are of great interest globally owing to their potential to act as sources and reservoirs of hydrocarbon accumulations [1,2]. However, due to the rising demand for energy, both marine and continental black shales have drawn more attention as conventional and unconventional petroleum resources [1–3]. Most of the black shale sediments contain appreciable

amounts of organic matter (more than 1 wt.%) and are mainly accumulated under anoxic bottom water conditions in the marine and continental sedimentary basins [4,5].

However, the diagenesis and accumulation of organic matter (OM) in these organic-rich shale sediments are seriously limited by several factors, such as biological productivity, continental weathering, sedimentation rates, clay mineralogy, water column oxygenation levels, sea-level change, and the sedimentary environment of these shales [6–9]. The productivity of organisms, together with the preservation and degradation of organic matter, are the most important factors responsible for organic matter enrichment [10–13]. Bioproductivity is one of the major factors controlling organic matter input, whereas the absence or depletion of dissolved oxygen in bottom waters fosters the preferential accumulation and preservation of OM in sediments [14–16]. In this regard, multi-integrated analytical methods are vital to the study of organic-rich shale systems, where organic and inorganic geochemistry combined with microscopic examination can be used to assess the origin of OM accumulation and their characteristics resulting from sedimentary factors influencing the OM accumulation [15,16].

The key focus of the present study is Rajasthan state, which is one of the largest hydrocarbon-containing sedimentary basins in western India (Directorate General of Hydrocarbons, India). Rajasthan is a part of the Indian Shield, which contains four basins, including the Barmer, Bikaner-Nagaur, Jaisalmer, and Sanchores Basins (Figure 1). These basins were developed by intracratonic sedimentation and are mostly located in the western part of Rajasthan. These basins include a sizable lignite resource that is mostly composed of thick organic-rich black shale partings, which are mainly found in the Paleocene–Eocene sequences [17,18].

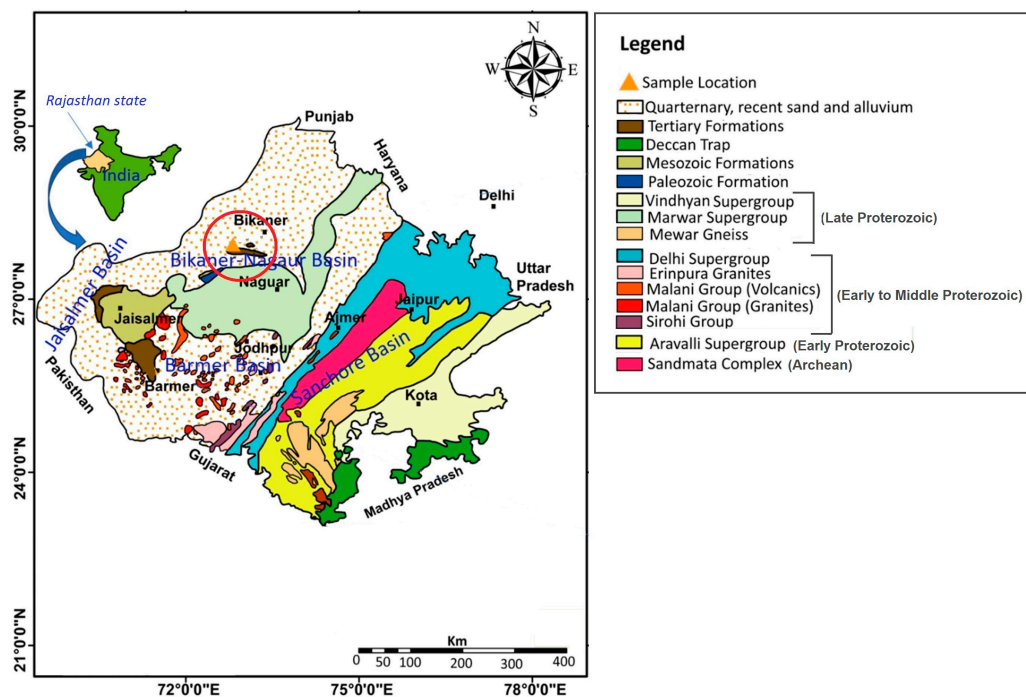


Figure 1. Geological map of Rajasthan showing the Gurha mine location in the Bikaner Nagaur Basin, northwestern India.

The current research focuses on the Paleocene–Eocene Palana Formation. In the Bikaner–Nagaur Basin, the Palana Formation has a thickness between 40 m and 120 m (Figure 2).

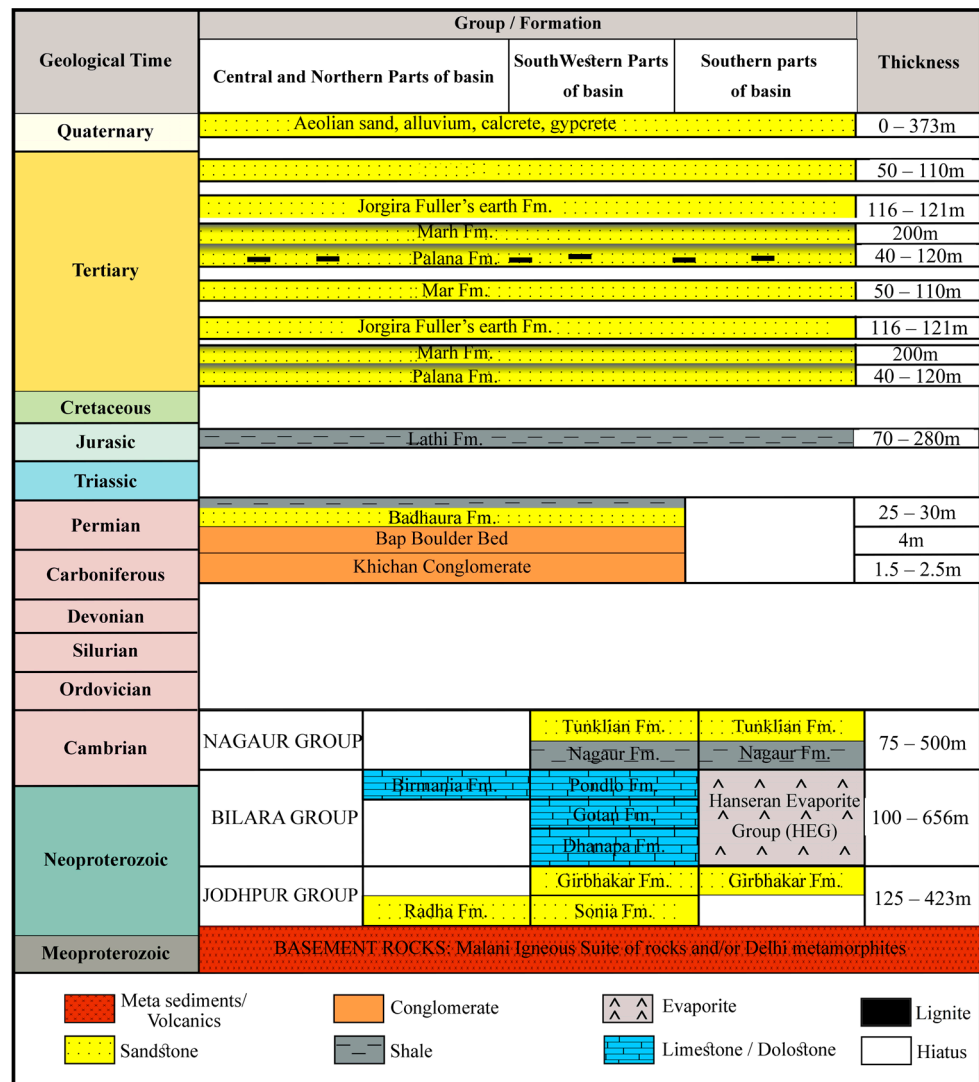


Figure 2. Generalized stratigraphic column in Bikaner–Nagaur Basin, including igneous rocks and sedimentary sequence (modified after Kumar and Chandra [19]).

The Palana Formation has attracted the attention of academia and exploration companies due to the presence of OM-bearing black shale sediments as superior source rocks and hydrocarbon generation potential. However, the lignite deposits in the Palana Formation have been extensively investigated by many researchers to characterize their organic matter and depositional setting and evaluate their hydrocarbon-generation potential [17,20–23] using advanced petrological and geochemical techniques. Notably, the associated black shale partings have received limited research attention [17] regarding their source rock characterization and hydrocarbon generation potential. A preliminary study suggested that Palana’s black shale deposits in the Gurha mines of the Bikaner–Nagaur Basin are enriched in sapropelic OM, with an unimportant admixture of humic and/or zoogenic substances locally, with mainly hydrogen-rich Types I and II kerogen, which have excellent potential for oil generation [17].

Although previous geochemical assessments have focused on the OM in the black shale facies within the Palana Formation and its potential for hydrocarbon generation [17], the questions about the influence of the depositional environment and the reasons for high organic carbon accumulation in the black shale rocks from the Palana Formation remain largely unclear.

The main objective of the current research is to understand the source of OM, depositional environment factors (i.e., upwelling, reducing, and warm climatic conditions),

and volcanogenic factors that influenced the high bioproductivity and organic carbon accumulation in the black shale rocks from the Palana Formation. The current study integrated previously published data from bulk organic geochemistry [17], with new findings from lithotype and mineral composition together with petrographical and geochemical characteristics of the black shale samples from the Palana Formation from the Gurha mine in the Bikaner–Nagaur Basin, western Rajasthan (Figure 1) using multi-techniques, including total organic carbon (TOC) and sulfur (S) contents, kerogen microscopy, quantitative evaluation mineral-scanning electron microscopy (QEMSCAN), X-ray diffraction (XRD), X-ray fluorescence (XRF), and scanning electron microscope (SEM) analyses.

2. Geological Setting

Rajasthan, which includes the Thar Desert in the northwest, is the largest state in India, accounting for 10.75% of the country's total land area [24].

In Rajasthan, four different sedimentary basins, including the Bikaner–Nagaur, Barmer, Sanchore, and Jaisalmer Basins, were developed due to intracratonic sedimentation, with an area of approximately 120,000 km² [25]. The sedimentary basins of Rajasthan comprise tectonic and lithological units spanning from the Archean to the Quaternary (Figure 1).

The Bikaner–Nagaur Basin was initially formed by extension along the Najd fault system of the Arabian plate during the late Proterozoic–early Cambrian period, as suggested by the paleogeographic reconstructions [26–28]. The western region of Rajasthan, including the Bikaner–Nagaur Basin, has evolved through Cretaceous and Jurassic tectonic events related to the separation of the Indian plate from the Gondwana supercontinent during the Mesozoic era [21,29]. However, a new tectonic event during the Cenozoic era has also been reported [30–33]. This is related to the Himalayan Mountains' development as a result of the Indian and Asian plates' reactive convergence and collision during the Paleocene–Eocene (Himalayan Orogeny) and the foreland basin of the Punjab in western India [33]. These tectonic events during the late Proterozoic–early Cambrian, Mesozoic, and Cenozoic periods led to the formation of several fault systems in the Bikaner–Nagaur Basin [26–28]. Most of the faults in the basin resulted from an initial phase of rifting as a result of the Pan-African orogeny during the Late Proterozoic [26–28]. However, this fault system in the basin witnessed multiple phases of reactivation as a result of younger tectonic episodes such as extension during the Permian–Triassic and early-to-mid Jurassic and compression during the Cenozoic. These fault systems in the Paleozoic, Mesozoic, and Cenozoic eras provided migration pathways for the potential rise of deep hydrothermal fluids.

However, the tectonic events during the late Proterozoic–early Cambrian, Mesozoic, and Cenozoic also led to the formation of thick Neoproterozoic and Lower Palaeozoic sediments with a maximum thickness of 1500 m [19], overlaid by a thin cover of upper Palaeozoic, Mesozoic, and Tertiary sediments (Figure 2). However, multiple phases of volcanic rock sequences and metasediment cycles occurred during the Precambrian. These phases form a banded gneiss structure that acts as the basement rock. These oldest basement gneiss rocks of the Archean age are collectively known as the Banded Gneissic Complex. The lithostratigraphic column of the Bikaner–Nagaur Basin is presented in Figure 2. This basin holds three groups of the sedimentary succession primarily from Neoproterozoic to early Cambrian in age, namely the Jodhpur, Bilara, and Nagaur groups (Figure 2). The sediments of these groups are a mixture of clastics, carbonates, and evaporites (Figure 2). The Jodhpur Group is the deepest sedimentary succession in the Bikaner–Nagaur Basin, which lies unconformably on the Precambrian basement rocks (Figure 2). The formations of the Jodhpur Group were mainly composed of sandstones. These formations were followed by the carbonate and evaporite sediments of the Bilara Group (Figure 2). The Cambrian Nagaur Group includes Nagaur and Tunklian formations, which comprise mainly sandstones for the Tunklian Formation and mainly shale for the Nagaur Formation (Figure 2).

The Nagaur Formation is unconformably overlain by the Bap beds, consisting of phyllite, gneiss, quartzite, and unmetamorphosed conglomerates [19]. Following the

deposition of the Bap beds, clastic (i.e., sandstone and shale) was deposited during the Permian, forming the Abu Badhaura Formation (Figure 2). The Badhaura Formation is overlain by a thin layer of shale from the Jurassic Lathi Formation, with unconformable contact (Figure 2).

Paleogene sediments are found internally in conformable contacts, such as the Jogira, Marth, and Palana Formations. The detailed lithological sequence of the Paleogene formations is illustrated in Figure 2.

The Paleocene–Eocene Palana Formation is the primary subject of this investigation, which is mainly composed of lignite with carbonaceous black shale and sandstone (Figure 2). The lignite-bearing Palana Formation in the Bikaner–Nagaur Basin includes land-derived spore–pollen assemblages, showing that the floristic linkage was tropical to subtropical and influenced by humid climatic conditions during peat accumulation [23]. The presence of flora assemblages in the Palana lignite sediments also suggests the presence of a mixed (i.e., rainforest/semi-arid/tropical evergreen) climatic condition in and around the mine area [34–36]. The presence of suboxic-anoxic environmental conditions during deposition of the Palana lignite and shale sediments was enough for accumulation and enhanced the growth of algae and other microorganisms in the black shale of the Palana Formation [17,23].

3. Materials and Methods

Nineteen black shale samples from the Paleocene–Eocene Palana Formation were collected from the exposed mine face of Gurha in the Bikaner–Nagaur Basin (Figure 3). In the Gurha mine, the overall thickness of the Palana Formation is approximately 25 m, which consists of a black shale sequence of approximately 8 m. In this case, each shale sample was collected at a distance of approximately less than 0.5 m, following the sampling method of Schopf [37]. The samples were subjected to multi-geochemical and petrological analyses, as highlighted in the next subsections.

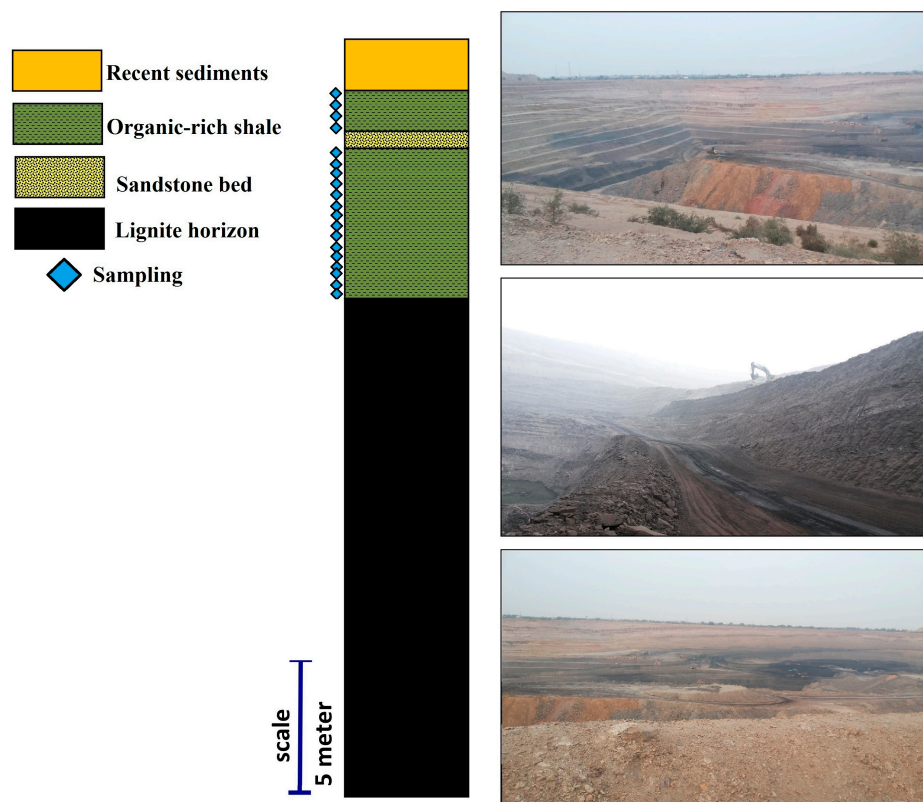


Figure 3. The lithology of the studied Gurha mine section, including the studied black shale horizons and photographs of the outcrop section.

3.1. Geochemical Analyses

Several geochemical measurements of TOC and S contents were carried out on the studied black shale samples of the Palana Formation from Gurha mine in the Bikaner–Nagaur Basin (Table 1). The collected samples were crushed into 72-mesh sizes using a mortar and pestle and then used for TOC and S content measurements. However, the preliminary geochemical results of TOC and S contents for most of the studied Palana shale samples (14 samples) are available from our prior published research by Singh et al. [17], and the other 5 new samples are added to the current study.

3.2. Optical-Microscopic Examinations

In this study, optical-microscopic examinations were conducted on the whole rocks using a standard polished block method using a reflected light microscope [38].

The collected samples were milled into ± 18 mesh (approximate ≤ 1 mm) sizes using a mortar and pestle. For embedding the shale particulates into pellet mounts, epoxy resin, an epoxy hardener, a release agent, and sample cups were used. The shale pellets were ground for 3–5 min with a polishing machine using different silicon carbide waterproof papers (mesh size: 180, 320, 600, 800, 1000, 1200, and 2000; speed: 150–180 RPM) under continuous slow water flow. Buehler MicroCloth (Buehler, Lake Bluff, IL, USA) and MicroPolish gel (0.05 micron) were used to polish the pellets. The polished blocks were then immersed in oil and studied under white reflected light and cross-polarized under UV light with a LEICA microscope (model DM6000M) (Leica Microsystems, Wetzlar, Germany), which had fluorescence illumination capabilities that enabled examination of the organic facies and differentiation of their assemblages.

3.3. Mineralogical and Elemental Composition Analyses

Various techniques are utilized to investigate the geochemical and mineralogical compositions, including both bulk and surface analyses using different types of samples.

The bulk analysis is conducted using X-ray fluorescence (XRF) and X-ray diffraction (XRD) techniques. In this case, ten black shale samples were crushed to less than 200 mesh and studied by an X-ray fluorescence (XRF) spectrometer using a PANalytical (EP-SOLON3X) XRF spectrometer (Malvern Panalytical, Malvern, Worcestershire, UK). The XRF analysis was used to determine the concentrations of the major oxides and trace elements in the studied black shale samples.

Additionally, the bulk mineralogy of the targeted samples is investigated using X-ray diffraction (XRD) with a Malvern PANalytical EMPYREAN Diffractometer (Malvern Panalytical, Malvern, Worcestershire, UK) system at two theta ranges of 2–70 and 0.01 step size. The acquired XRD data were processed using X'Pert Highscore software. Qian et al. [39] and Amao et al. [40] illustrated and discussed the concepts and experimental design of such a technique.

For surface analysis, three polished shale samples were analyzed to obtain more detailed information about the mineralogical and geochemical composition of specific spots by scanning electron microscopy (QEMSCAN), including species identification (SPI), scanning electron microscopy (SEM), and energy dispersive spectroscopy (EDS). The QEMSCAN analysis is used to scan the sample with an electron beam and analyze the backscattered electrons to determine the mineralogical and geochemical composition of selected spots. The concepts, workflow, and applications of QEMSCAN are discussed in the literature, including Qian et al. [39], Ayling et al. [41], and Alqubalee et al. [42].

Table 1. Geochemical results of the analyzed black shales in the Paleocene–Eocene Palana Formation in western Rajasthan, India, including total organic carbon (TOC) and total sulfur (TS) content and bulk mineral composition from XRD analysis.

Basin Mine	Samples ID	TOC Wt.%	TS Wt.%	Bulk Mineral Compositions (XRD Results)																								
				Silica Minerals					Clay Minerals					Carbonate Minerals			Heavy Minerals				Other Minerals							
				Quartz	Olivine	Apophyllite	Tri-dymite	Albite	Total	Kao-linite	Dickite	Muscovite	Zeolite	Total	Calcite	Cerussite	Total	Anatase	Zircon	Clinopyroxene	Ilmenite	Rutile	Total	Gypsum	Apatite	Pyrite	Total	
Bikaner-Nagaur Basin Gurha	BSG-1	21.75	1.90																									
	BSG-2	30.69	1.80																									
	BSG-3	29.75	2.10																									
	BSG-4	32.40	1.90																									
	BSG-5	29.41	1.70																									
	BSG-6	18.23	2.18	11.7	1.17			7.8		20.67	14.7	11.8		2.0	33.4		1.0	1.0	1.0	2.0	3.9	2.0		8.9	19.6		2.9	22.5
	BSG-7	25.26	1.70	16.0	2.50					18.50	19.0			4.0	23.0	3.0	2.0	5.0	3.0	4.0	7.0		2.0	16.0	7.0	8.0		15.0
	BSG-8	30.30	1.84																									
	BSG-9	31.08	1.79	4.0	2.93	13.1	7.1			27.13	27.3	19.2			46.5													
	BSG-10	30.04	2.04	9.0	2.90			7.0		18.90	8.0	21.0	15.0	2.0	51.0	2.0	1.0	3.0		2.0	7.0			9.0	4.0	4.0	4.0	12.0
	BSG-11	29.46	2.24	3.9	3.00			8.8		15.70	22.5	19.6		2.0	44.1		2.0	2.0	2.9					2.9			7.8	7.8
	BSG-12	28.57	2.12																									
	BSG-13	36.23	1.72	13.0	2.30	8.0	11.0			34.30	24.0	17.0		2.0	43.0				2.0					2.0				
	BSG-14	26.73	1.63	2.0	3.20				9.1	14.30	14.1			16.2	6.1	36.4		1.0	1.0	2.0	1.0		2.0	3.0	8.0			
	BSG-15	32.09	1.55	10.8						10.80	21.6	15.7	19.6	2.9	59.8	2.9		2.9	3.9	2.9	12.7			19.5	6.9			6.9
	BSG-16	28.64	1.85																									
	BSG-17	33.04	1.74	19.8	5.00			5.9		30.70	15.8	11.9		3.0	30.7		1.0	1.0						13.9	20.8			34.7
	BSG-18	29.57	2.09																									
	BSG-19	4.04	1.91	42.0	2.00	3.0	5.0			52.00	5.0	6.0		1.0	12.0		1.0	1.0	1.0		4.0	1.0		6.0	24.0	4.0	2.0	30.0

4. Results

4.1. Total Organic Carbon (TOC) and Sulfur (S) Contents

The presence of organic matter in sediments is commonly inferred by the organic carbon content (TOC), which is conventionally reported as a function of weight percent. In this regard, the studied black shales of the Paleocene–Eocene Palana Formation are enriched by OM with TOCs ranging between 4.04 and 36.23 wt.% (Table 1). Most of the measurements indicate TOC > 10 wt.% (18.23%–36.23%), as shown in Table 1. The high amount of OM points towards a reducing environmental condition during the deposition of these studied black shale sediments. However, the conditions are constrained using other geochemical data, which are detailed in the following sections.

In addition, the sulfur content in the studied shale samples ranges from 1.55 wt.% to 2.24 wt.% (Table 1). The S content usually differentiates between marine and -non-marine environments [43]. High S content (i.e., >1 wt.%) denotes a marine environment [15,43,44], which is the case for the Palana black shale facies. However, the relationship between TOC and S contents also agrees that the analyzed black shales generally fall within the normal marine environmental setting (Figure 4).

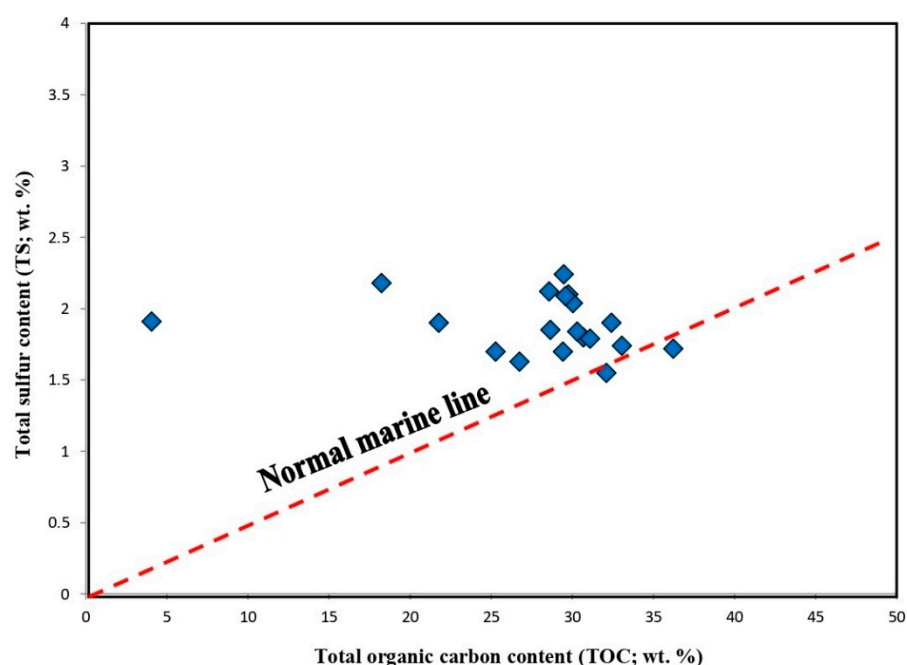


Figure 4. The relationship between TOC and TS contents for the studied black shale samples of the Palana Formation showing a normal marine environmental setting (after Hedges and Keil [44]).

4.2. Organic Facies Characteristics

Organofacies of the studied black shale samples of the Palana Formation in the Gurha (Bikaner–Nagaur Basin) were identified using microscopic investigation under UV radiation reflected light, as shown in Figure 5. The organofacies are dominated by high amounts of liptinite, with small amounts of huminite maceral from the terrestrial organic matter (Figure 5). The liptinite maceral in the studied shale samples is presented as structured and unstructured organic matter, including alginite, sporinite, and resinite, which are characterized by fluorescence emission colors ranging from orange to yellow (Figure 5). However, the hydrogen-rich liptinites display a high abundance of alginite, and they were classified into telalginite and lamalginite based on their morphologies (Figure 5a–e). Telalginite arises from algae and occurs as fan-shaped, flattened discs and discrete lenses (Figure 5a,b), whereas lamalginite occurs as thick lamellae (Figure 5c–e). In addition, most of the sporinites in the black shale samples occur as thin-walled, isolated microspores (Figure 5e,f). Other unstructured macerals, such as resinite, also occurred in the studied

shale samples (Figure 5). The resinite appears to be rounded, oval, and laminar-shaped (Figure 5g,h).

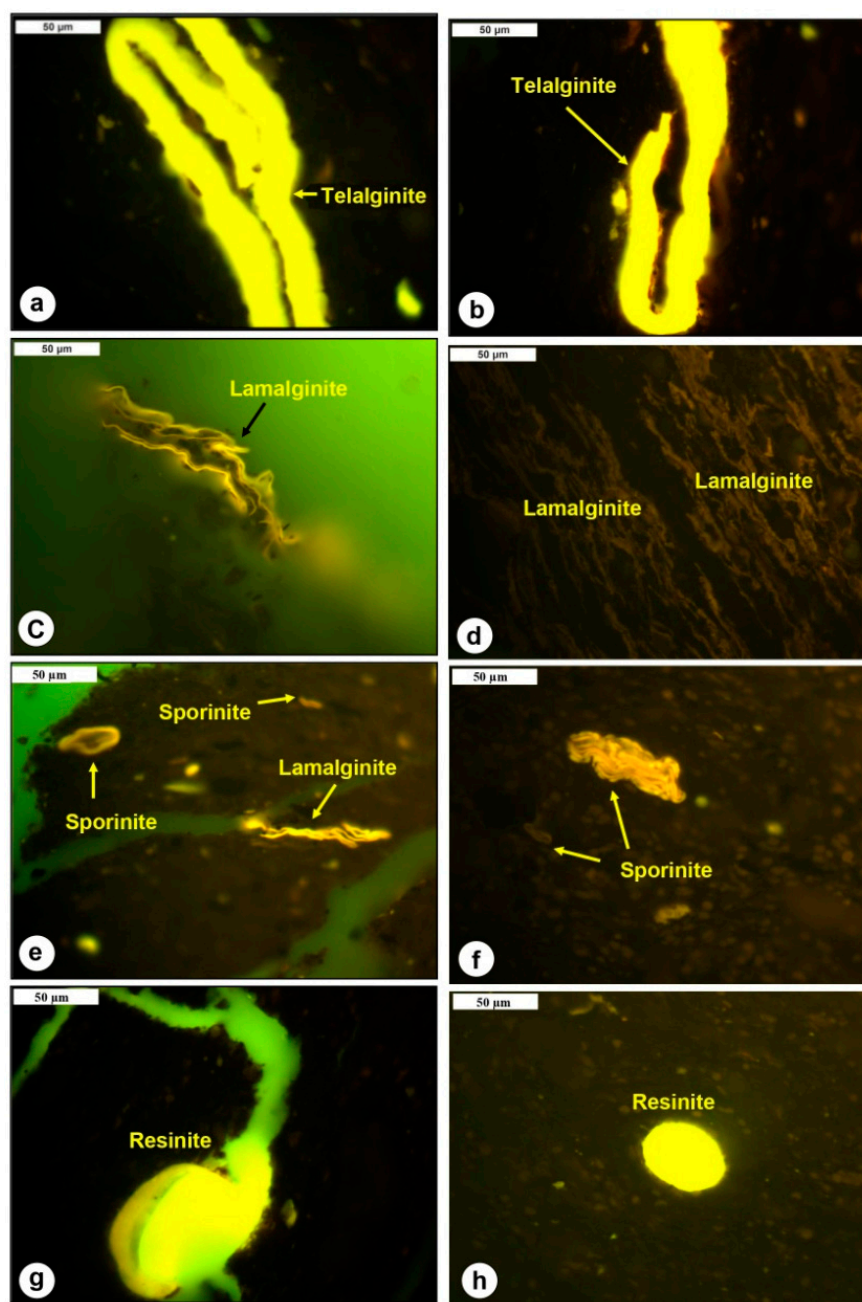


Figure 5. Photomicrographs of the studied black shale samples of the Palana Formation under reflected UV light with a field width of 0.2 mm, including different organic matter assemblages of liptinite such as alginite, sporinite, and resinite ((a–c) from the BSG-9 sample, (d) from the BSG-6 sample, and (e–h) from the BSG-11 sample).

4.3. Mineralogical Composition and Lithotype

The bulk mineral compositions of the analyzed black shale samples from the Palana Formation were primarily determined by the XRD results coupled with QEMSCAN results for the surface of the samples. According to the mineral composition distributions in the XRD results, the clay (12.41%–59.8%) and silicate (10.8%–52.0%) minerals prevail over the carbonates (1%–5%), with significant amounts of heavy minerals (2.0%–19.5%) and other minerals (6.9%–34.7%), including gypsum, apatite, and pyrite (Table 1). Most of the clay

minerals in the Palana black shale samples are kaolinite and dickite, with muscovite and some zeolite, while the silica minerals comprise quartz, olivine, and other silica minerals (i.e., apophyllite, tridymite, and albite). However, the prevalence of clay (12.41%–59.8%) and silica (10.8%–55.0%) minerals in the Palana black shale samples is inferred as mainly a clay-rich siliceous mudstone lithotype with silica-rich argillaceous mudstone and silica-dominated lithotypes (Figure 6).

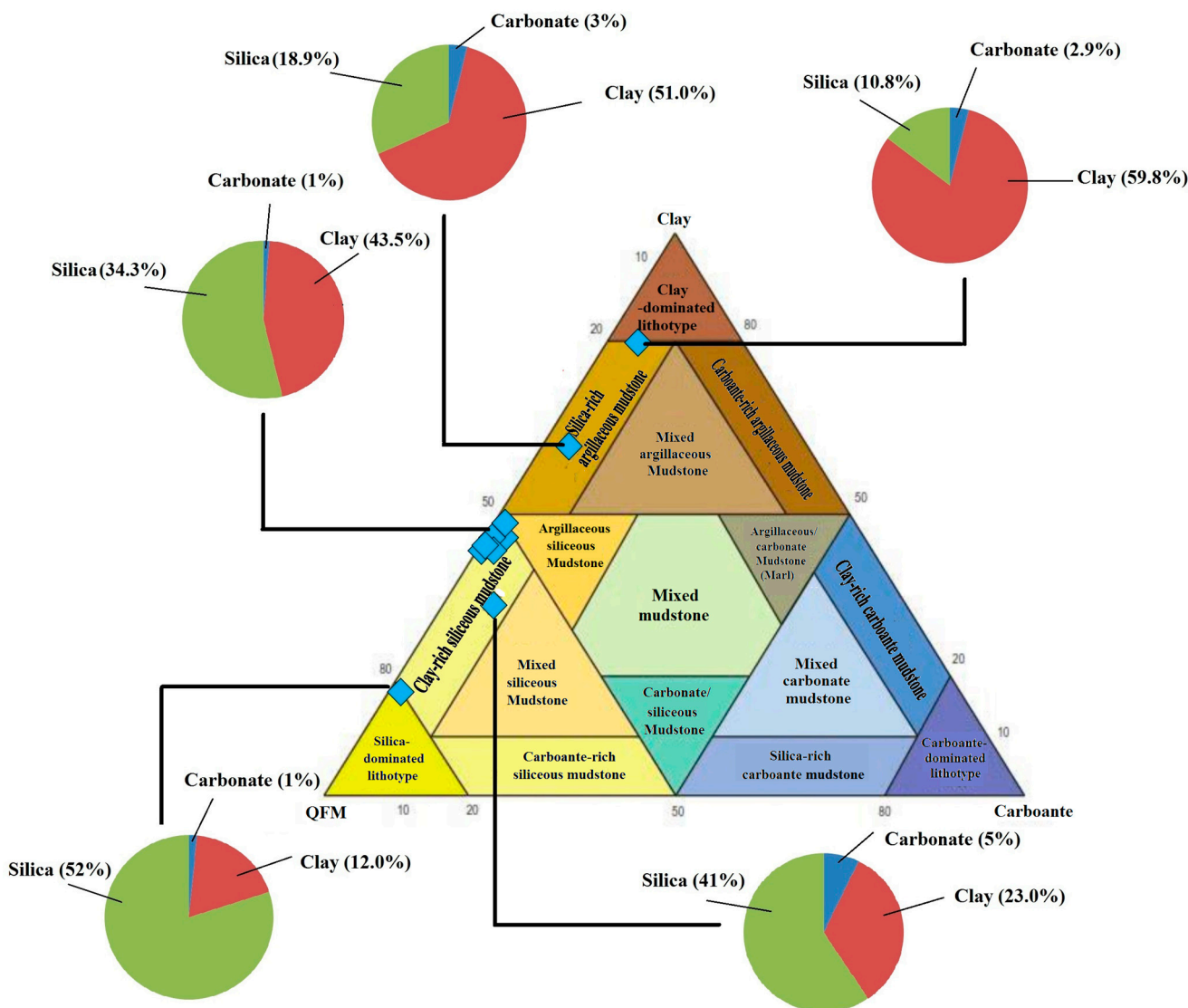


Figure 6. Ternary plot of the comparison of silica, carbonate, and clay contents showing lithology types of the studied black shale samples of the Palana Formation (modified after Dowey and Taylor [45]).

Such enrichment with clay and quartz minerals is also clearly demonstrated from the species identification (SPI) of the QEMSCAN results (Figure 7). The QEMSCAN results also deciphered that the Palana shale facies contains mainly organic matter associated with siderite, gypsum, pyrite, and heavy minerals (Figure 7). In addition, the SEM results also revealed that the analyzed Palana shale samples contain common clay minerals (Figure 8A), including kaolinite, dickite, and chlorite (Figure 8A-1,A-2). The presence of barite was also observed in the studied samples in the form of fabric (Figure 8B-1), associated with organic matter (Figure 8B-2,B-3), and framboidal pyrite (Figure 8C-1). The occurrence of foraminiferal assemblages in the studied samples (Figure 8C-2) suggests a marine environment. The marine setting is also demonstrated by the presence of the coccolithophore

plankton (i.e., *Zeugrhabdotus erectus* Sp.; Figure 9A), which is regarded as marine algae. The SEM also shows that the fabric barite is mainly associated with algal- and bacterial-derived organic matter (Figure 9B,C). From this point of view, the presence of barite in the studied shale samples may have formed as a replacement for the gypsum due to bacterial mediation in a humid climate [46,47].

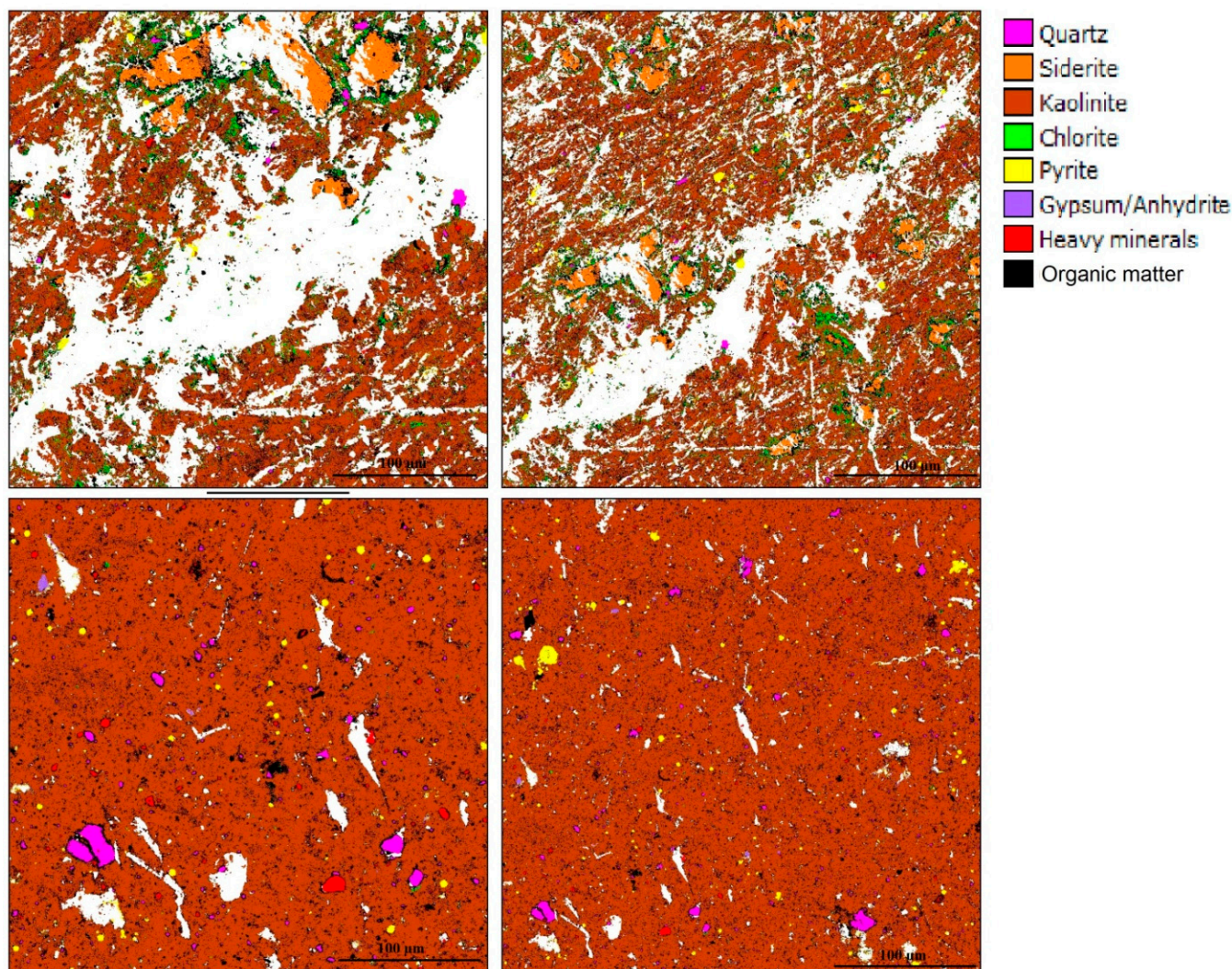


Figure 7. QEMSCAN image showing the mineral compositions and associated organic matter in the studied samples of black from the Palana Formation (from the BSG-9 and BSG-13 samples).

4.4. Major and Trace Elements Composition

The abundances of major oxides and selected trace elements, as well as their ratios, are presented in Table 2. Most of the studied Palana shale samples are higher in SiO_2 (42.49%–51.69%), Al_2O_3 (26.68%–32.22%), and significant amounts of Fe_2O_3 (8.61%–22.68%), while they are depleted in TiO_2 , SO_3 , CaO , MgO , P_2O_5 , Na_2O , and K_2O , respectively (Table 2).

The correlation between the Fe_2O_3 and SO_3 , as indicated by the cross-plot Fe-S, shows that the high concentrations of the Fe_2O_3 in most of the samples plotted to the right of the pyrite defined line (Figure 10A), indicating that pyrite is not the main source of the Fe fraction in the analyzed samples, suggesting other sources like olivine. The XRD results confirm that olivine is also present in the analyzed shale samples (Table 1); thus, olivine is the main source of Fe, as clearly demonstrated by the direct proportional relationship between Fe_2O_3 and olivine, as shown in Figure 10B.

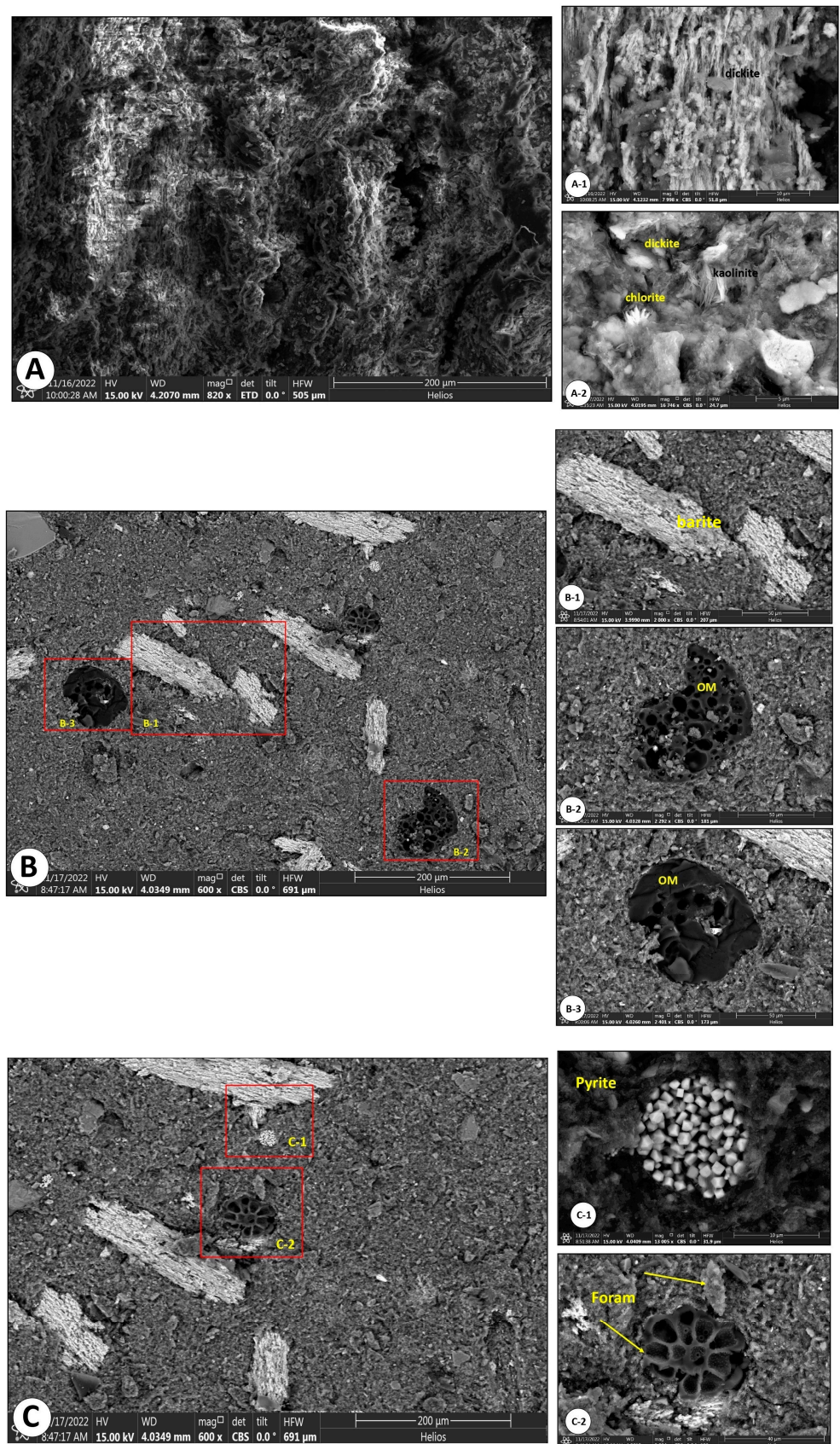


Figure 8. SEM photomicrographs showing the mineral composition and associated organic matter in the studied samples of black shale from the Palana Formation (from the BSG-9, BSG-13, and BSG-15 samples).

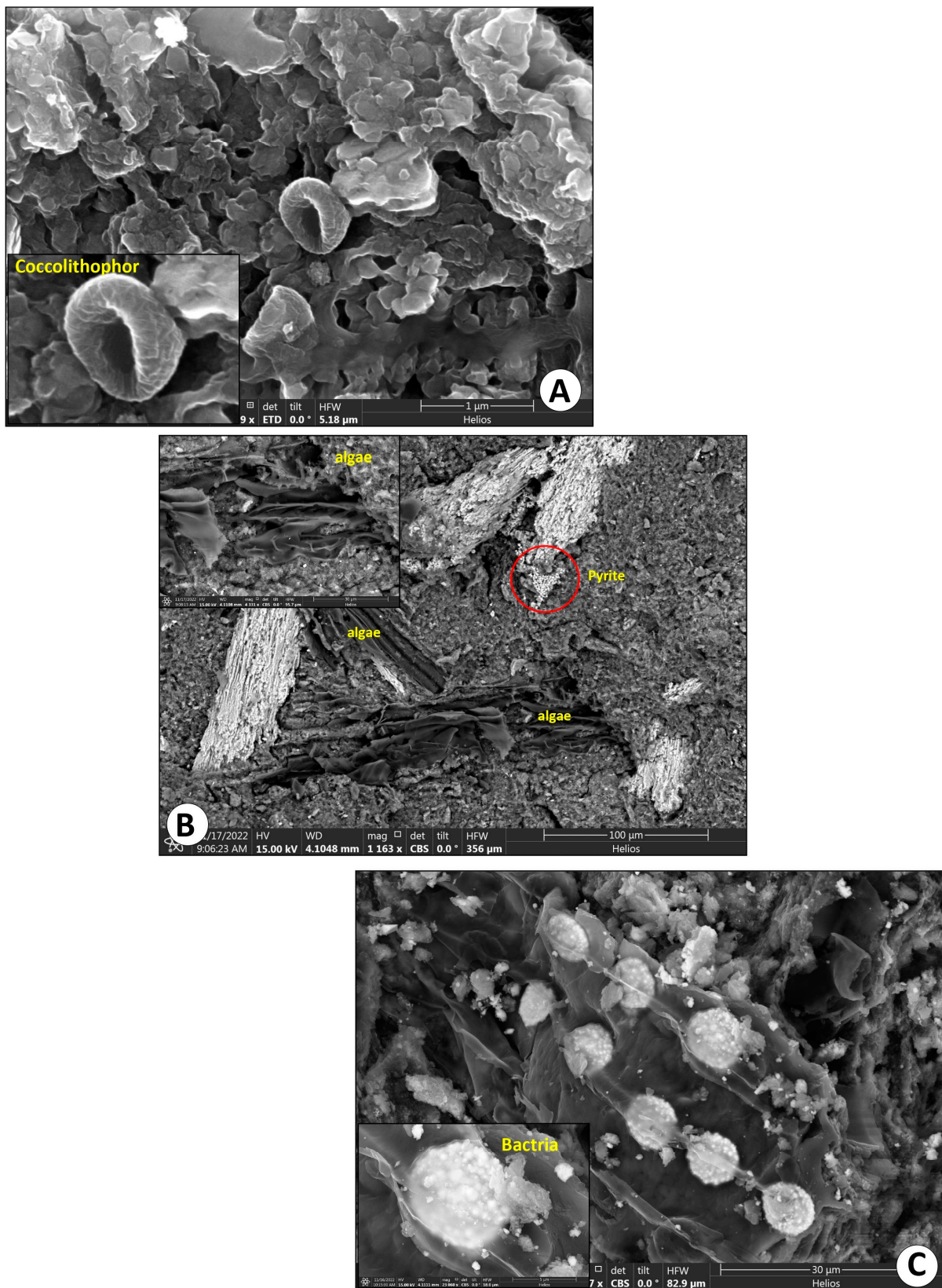


Figure 9. SEM photomicrographs exhibiting the organic matter input in the studied samples of black shale from the Palana Formation (from the BSG-9, BSG-13, and BSG-15 samples).

Table 2. Inorganic data (X-ray fluorescence analysis), including major oxides (%) and trace elements (ppm) of the analyzed black shales of the Paleocene-Eocene Palana Formation in western Rajasthan, India.

Sample ID	Major Oxides (%)														Trace Elements (ppm)																								
	SiO ₂	Al ₂ O ₃	CaO	Fe ₂ O ₃	K ₂ O	MgO	P ₂ O ₅	TiO ₂	Na ₂ O	SO ₃	MnO	Al/K	K/Al	Ca/Mg	Fe+Mn/Ti	100* Mg/Al	CIA	PIA	V	Cr	Co	Ni	Cu	Zn	Ga	Rb	Sr	Zr	Cd	Ba	Rb/Sr	V/Ni	V/V+Ni	V/Cr	Sr/Cu	Sr/Ba	Ga/Rb	Co* Mn	
BSG-6	46.58	31.31	1.45	13.20	0.12	0.46	0.25	3.64	0.24	1.97	0.01	260.9	0.004	3.15	13.20	1.47	94.54	94.90	1690	637.9	588.4	233.3	497.1	199.9	68.6	6.8	380.1	830.8	9.2	166.1	0.02	7.24	0.88	2.65	0.76	2.29	10.09	0.0006	
BSG-7	43.44	30.22	1.40	18.59	0.08	0.47	0.40	3.71		1.12	0.02	377.8	0.003	2.98	18.60	1.56	95.33	95.58	1660	647.8		258.7	438.6	154.6			582.4	825.8				6.42	0.87	2.56	1.33				
BSG-9	51.69	31.23	1.41	15.95	0.27	0.74	0.14	3.30	0.30	1.70	0.01	115.7	0.009	1.91	8.61	2.37	94.04	94.85	1550	590.5	391.3	220.2	435.5	292.0	73.2	21.7	347.5	786.4	39.6	206.2	0.06	7.04	0.88	2.62	0.80	1.69	3.37	0.0004	
BSG-10	43.40	26.68	1.14	22.86	0.18	0.61	0.22	2.61	0.27	1.47	0.02	148.2	0.007	1.87	22.87	2.29	94.38	95.01	1090	470.9	1050	139.8	312.3	180.2	46	15.6	276.7	606.5	26.0		0.06	7.80	0.89	2.31	0.89		2.95	0.0021	
BSG-11	46.53	31.27	1.63	12.95	0.10	0.51	0.29	3.48	0.24	2.24	0.01	312.7	0.003	3.20	12.95	1.63	94.07	94.37	1620	628.3	596.3	247.0	502.5	226.5	73.3	7.3	509.1	782.2	27.3	233.2	0.01	6.56	0.87	2.58	1.01	2.18	10.04	0.0006	
BSG-13	48.48	30.22	1.45	11.20	0.19	0.40	0.28	3.14	0.24	1.27	0.02	159.1	0.006	3.88	11.21	1.32	94.14	94.74	1590	537.6	598.4	223.3	397.1	299.9	68.6	7.8	280.1	850.8	28.8	186.1	0.03	7.12	0.88	2.96	0.71	1.51	8.79	0.0012	
BSG-14	42.49	32.22	1.60	15.59	0.09	0.57	0.50	3.51	0.33	1.32	0.02	358.0	0.003	2.81	15.60	1.77	94.10	94.36	1060	447.8	578.4	368.7	438.6	184.6	78.0	13.7	592.4	725.9	20.7	210.8	0.02	2.87	0.74	2.37	1.35	2.81	5.69	0.0012	
BSG-15	50.79	31.23	1.51	9.61	0.29	0.78	0.19	2.80	0.39	1.60	0.01	107.7	0.009	1.94	9.61	2.50	93.45	94.31	1650	580.4	491.3	240.5	415.5	299.8	65.2	23.7	357.5	656.4	35.6	209.2	0.07	6.86	0.87	2.84	0.86	1.71	2.75	0.0005	
BSG-17	45.90	29.65	1.24	18.86	0.22	0.69	0.32	2.91	0.29	1.57	0.02	134.8	0.007	1.80	18.87	2.33	94.43	95.13	1190	570.8	1090	159.2	212.3	150.5	46.0	17.6	256.7	696.5	29.5	143.2	0.07	7.47	0.88	2.08	1.21	1.79	2.61	0.0022	
BSG-19	49.83	28.27	1.23	8.61	0.08	0.61	0.31	3.18	0.26	2.34	0.01	353.4	0.003	2.51	15.95	2.16	94.74	95.01	1520	648.3	496.3	217.5	509.5	236.9	35.3	10.3	518.1	882.1	9.2	243.2	0.02	6.99	0.87	2.34	1.02	2.13	3.43	0.0005	

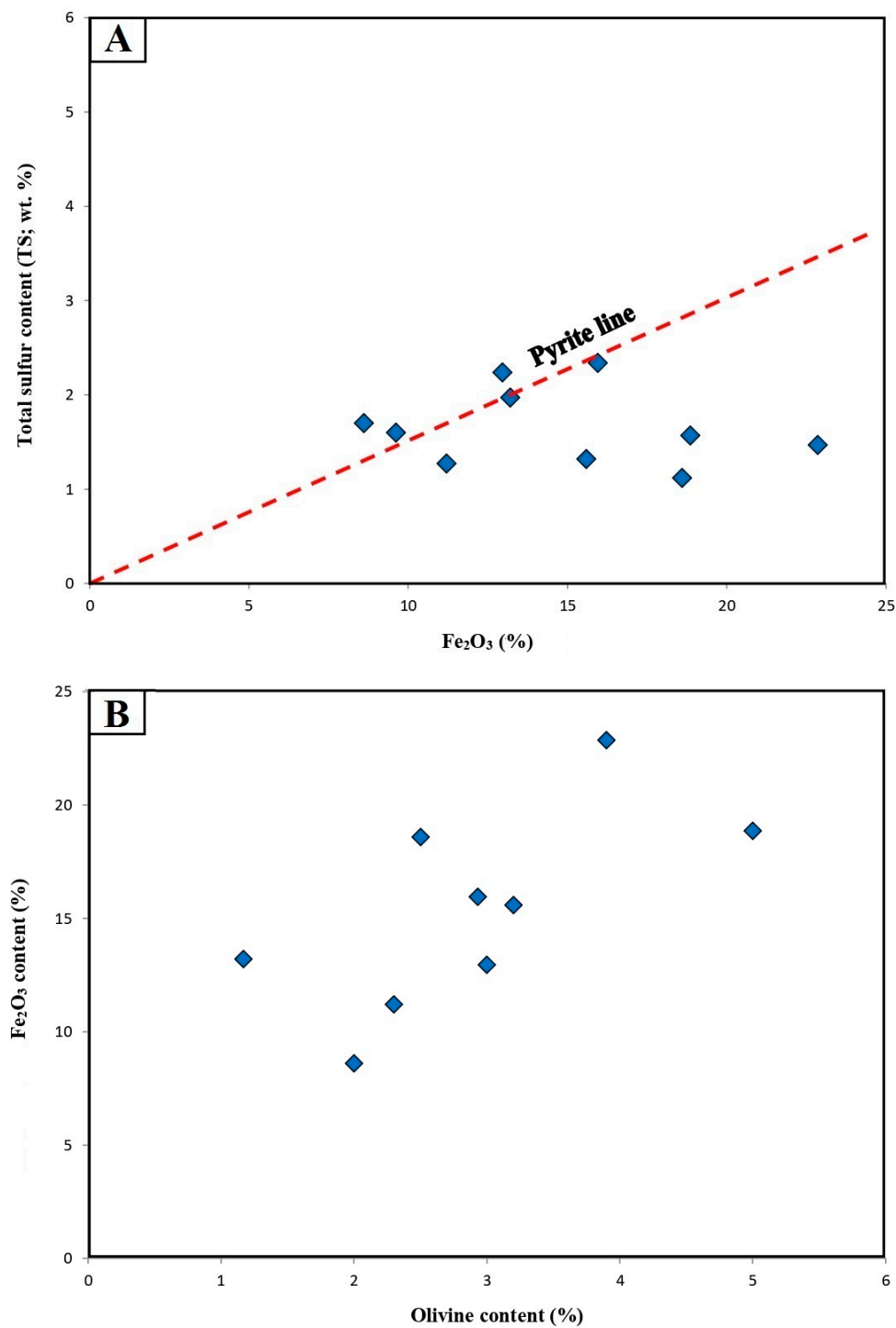


Figure 10. (A) Relationship between the Fe_2O_3 and TS contents (after Algeo and Maynard [48]); (B) Fe_2O_3 versus olivine contents in the studied samples of black shale from the Palana Formation, showing that the Fe element is mainly sourced from olivine.

The presence of the Si, Al, Fe, Ti, S, Ca, Mg, Na, Mn, and K elements, associated with organic carbon (C), is also supported by the EDS results from the studied black shale samples of the Palana Formation, as shown in Figure 11.

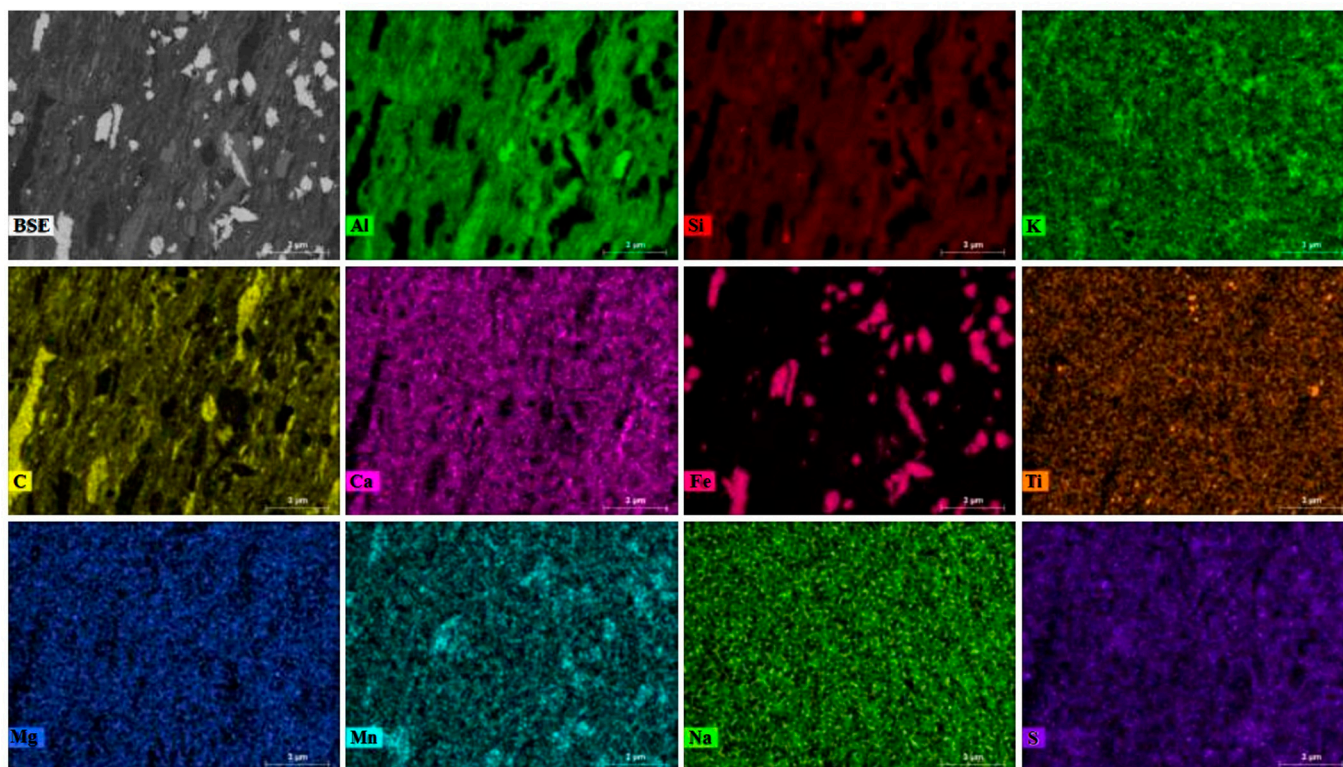


Figure 11. Major elements in the studied samples of black shale from the Palana Formation identified using EDX spectra of the surface of the sample (from the BSG-15 sample).

Furthermore, the analyzed Palana shale samples show enrichment with V, Ni, Cr, Co, Cu, Zr, Zn, Sr, and Ba trace elements (Table 2). The observed enrichment of trace elements in the studied samples, especially V, Ni, and Sr, is suggestive of a marine environment [49].

The Palana samples also contain other trace elements in low amounts, such as Ga, Cd, and Rb, respectively (Table 2). However, several geochemical ratios, such as V/Ni, V/(V+N), V/Cr, Sr/Cu, Sr/Ba, and Ga/Rb, are in the ranges of 2.87–7.80, 0.74–0.89, 2.08–2.96, 0.71–1.35, 1.51–2.81, and 2.61–10.09, respectively (Table 2). These ratios derived from trace elements are commonly used to assess the paleoredox and paleoclimate conditions, as discussed in the next subsections.

5. Discussion

5.1. Sedimentary Depositional Environment during the Paleocene–Eocene

The knowledge and information of the sedimentary depositional environment of the black shales in the Palana Formation during the Paleocene–Eocene were studied by employing multiple proxies, including elemental data, together with kerogen microscopy. In this case, the sedimentary depositional environments and their impact on organic matter accumulation in the black shale of the Palana Formation are discussed based on three main factors, including paleoredox conditions, paleosalinity, and upwelling action.

The organic carbon accumulation and its preservation condition during deposition are directly linked to the paleoredox conditions [7,14,50]. The paleoredox conditions are divided into four levels based on the concentration of dissolved O₂ in bottom water, as follows: oxic, dysoxic, anoxic non-sulfidic, and anoxic sulfidic (euxinic) conditions.

In this study, anoxic conditions (low oxygen) during the Paleocene–Eocene period were recognized based on the high amount of OM in the black shale facies of the Palana Formation, with TOC up to 36.23 wt.% (Table 1), which increased the effective preservation and resulted in organic enrichment. The finding of the anoxic condition (low oxygen) during the Paleocene–Eocene is established using redox-sensitive trace elements (i.e., Ni, V, and Cr) and their ratios as redox proxies [51].

The V and Ni trace elements are commonly insoluble and are enriched under reducing environmental conditions, whereby they can be used as redox-sensitive indicators for anoxic environmental conditions [48,51,52]. In this case, the V concentration is higher than Ni in the black shale facies of the Palana Formation, indicating that marine anoxic environmental conditions were promoted during the Paleocene–Eocene, as indicated by the relationship between the V and Ni (Figure 12A). The anoxic environmental conditions during the accumulation of the Palana black shale facies can also be determined by V/Ni and V/(V+Ni) ratios [53,54]. The V/Ni ratio has been used by Galarraga et al. [53] as an indicator for the interpretation of paleoredox conditions. According to this work, a V/Ni ratio of <2 indicates an anoxic condition, while V/Ni ratios of >1 indicate deposition under oxic conditions. Generally, the values of the V/Ni ratio recorded in the shale samples from the Palana Formation are higher than 2 (Table 2), further suggesting anoxic conditions during the deposition of these shale sediments. Moreover, the V/(V+Ni) ratio of the Palana shales under investigation is between 0.74 and 0.89, indicating anoxic environmental conditions during the deposition [54]. This interpretation is also demonstrated by the association between the V/(V+Ni) ratio and TS content, which alludes to marine anoxic environmental conditions (Figure 12B).

In addition, the V/Cr ratio is also commonly used to provide information on the oxygenation conditions in the environment of deposition [55]. Jones and Manning [55] suggested that a V/Cr ratio higher than 4.5 shows anoxic conditions were predominant, while a V/Cr ratio less than 2 indicates oxic conditions. Accordingly, the values from the Palana shale samples are $2 < V/Cr < 4.5$ (Table 2), resulting in anoxia beginning with less prevalence during the period of their deposition. However, this study integrates the organic matter content and enrichment in elements such as S and Fe to assess the environmental conditions during deposition time, as reported by Algeo and Liu [56]. In this regard, the concentrations of Fe_2O_3 and S, together with TOC content, were plotted on a Fe_2O_3 -TOC-S ternary diagram and generally show that the Palana black shale samples were plotted in the zone of low oxygen conditions, as shown in the ternary diagram of Arthur and Sageman [57] (Figure 13). The anoxic depositional setting (low oxygen) of the Palana black shale facies during the Paleocene–Eocene was also recognized based on the isoprenoid distributions and their narrow Pr/Ph ratio of less than 0.60 [17], where low O_2 conditions promote Ph enrichment when compared to Pr [58].

Therefore, these Paleocene–Eocene anoxic environmental conditions contribute to the preservation of OM and maximize the effect of OM's accumulation during the deposition of the organic-rich shale sediments of the Palana Formation.

Furthermore, reconstruction of the paleosalinity condition is another important factor that greatly helps in understanding the mechanism of organic carbon enrichment, including the biological community and anoxic conditions of the water column [59].

In this study, salinity-sensitive elements in the studied Palana black shale facies, including Ca, Mg, and Al, were used to assess the salinity condition during the Paleocene–Eocene depositional time [60–62]. In this regard, the Sr and Ba trace elements and their ratios of Sr/Ba (Table 2) are mainly used as an indicator for salinity and/or evaporation conditions [63–67]. The high concentrations of Sr indicate high salinity and/or evaporation conditions during the deposition of the sediments, with high values of the Sr/Ba ratio [59,68]. Accordingly, a preliminary investigation of the studied Palana black shale facies indicates that it was deposited in relatively high salinity stratification with a high relative Sr/Ba ratio between 1.51 and 2.81 (Table 2).

This finding is also consistent with the Sr/Ba ratio versus V/Ni ratio diagram, as the salinity stratification of the water columns regulates the anoxic conditions during the deposition of Palana shale sediments (Figure 14A). This interpretation is also corroborated by the association between the Ca, Mg, and Al elements and their $100 \times Mg/Al$ and Ca/Mg ratios [69,70]. In this case, a low $100 \times Mg/Al$ ratio of <1 usually indicates freshwater conditions, while values $1 < 100 \times Mg/Al < 10$ suggest normal seawater, and a $100 \times Mg/Al$ ratio of >10 implies high salinity—seawater in hypersalinity deposition conditions [69,70].

In our case, the studied black shale facies in the Palana Formation exhibits $100 \times \text{Mg}/\text{Al}$ ratios between 1.32 and 2.5 (Table 2), indicating that it was deposited in a moderate salinity (normal seawater) condition during the Paleocene–Eocene, as demonstrated by the relationship between sulfur content and relatively high values of the Ca/Mg ratio in the range of 1.8–3.88 (Figure 14B). However, the availability of the nannofossil taxa, i.e., *Zeugrhabdotus erectus*, in the Palana shale samples (Figure 9A), was used as an indicator for shelf species [71–73], where a condition of warm normal-salinity seawater was prevailed.

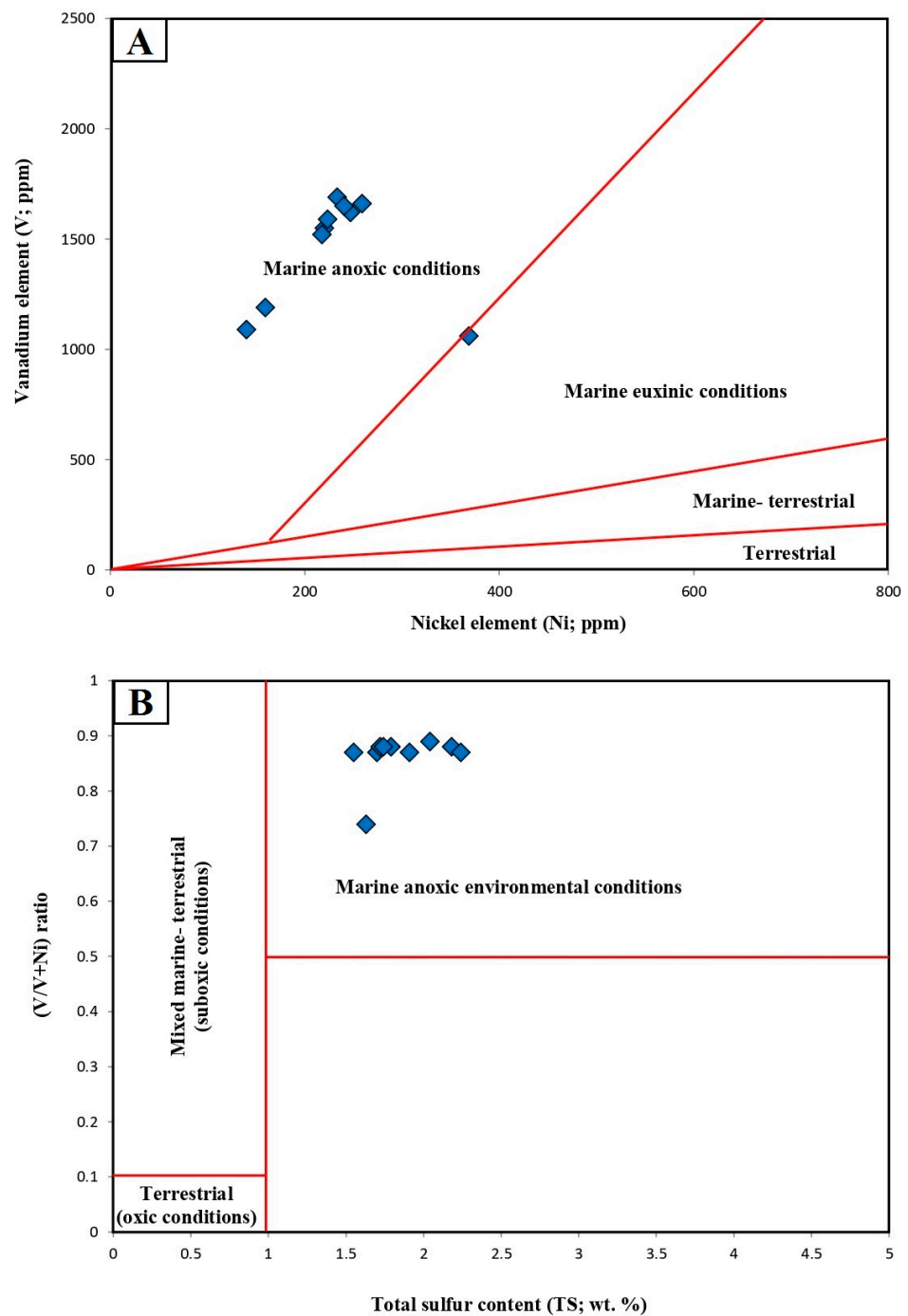


Figure 12. Geochemical correlations of (A) V and Ni trace elements (after Galarraga et al. [53]) and (B) total sulfur (TS) and V/(V+Ni) ratio (after Bechtel et al. [52]) indicating high-marine-reducing environmental conditions during deposition (Paleocene–Eocene) in the studied samples of the black shale from the Palana Formation.

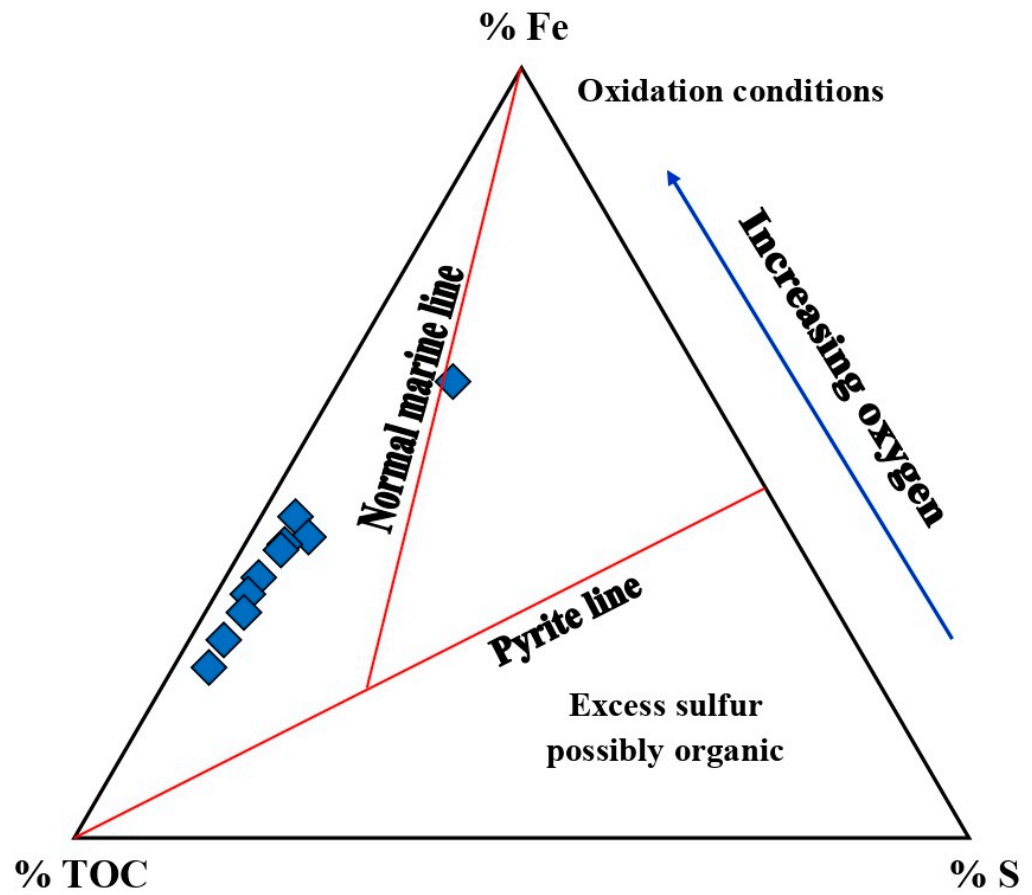


Figure 13. Ternary Fe_2O_3 -TOC-S ternary diagram of the studied samples of the black shale from the Palana Formation, further showing low oxygen content (anoxic conditions) during deposition (modified after Arthur and Sageman [57]).

In addition, upwelling processes affect the periodic influx of large masses of nutrients into the photic zone, and bioproductivity is closely related to nutrient supply in the sea [74,75].

Currently, a number of inorganic geochemical elements such as Mo, Cd, Mn, and Co have been used to indicate the impact of the vertical circulation of sea water (upwelling systems) on the sedimentogenesis of black shale [76–79]. In this case, upwelling zones show low abundances of both Co and Mn elements, while the contents of Co and Mn are relatively high in restricted basins [77]. This may be attributed to an insufficient fluvial input supply in regions affected by upwelling systems [77], where the Co and Mn enrichment in marine sediments is controlled by detrital input and authigenic enrichment [80]. The $\text{Co} \times \text{Mn}$ module has been developed to show that values above 0.40 indicate limitation in a marine basin, and $\text{Co} \times \text{Mn}$ below 0.4 is typical for upwelling conditions.

In this study, high upwelling conditions during the Paleocene–Eocene period were recognized based on the $\text{Co} \times \text{Mn}$ beginning smaller than 0.40 (0.004–0.22). This interpretation is corroborated by the association between the $\text{Co} \times \text{Mn}$ module and the Al_2O_3 content, as shown in Figure 15A. Similarly, the relatively high Cd content, together with an increase in organic matter in the studied black shales from the Palana Formation, indicates upwelling processes in water bodies with high primary bioproductivity during the deposition period [81]. This finding is clearly matched with the direct proportionality between the Cd and TOC contents (Figure 15B). In addition, the evidence of upwelling deposition is the presence of phosphates, as indicated by the high P_2O_5 of up to 0.50% in the studied Palana shale samples (Table 2).

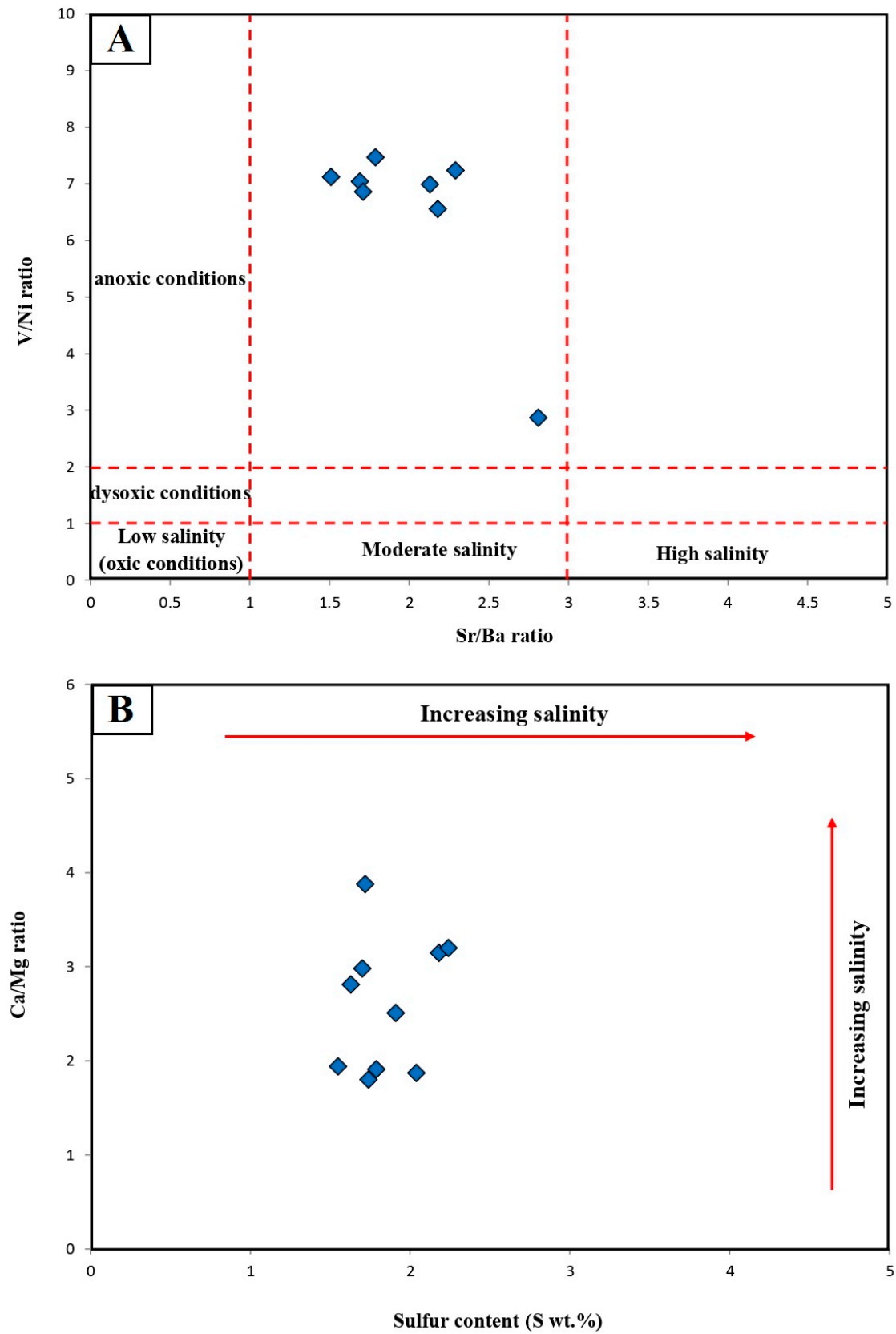


Figure 14. (A) Relationship between Sr/Ba and V/Ni ratios, and (B) Ca/Mg vs. $100 \times \text{Mg}/\text{Al}$ ratios plot showing normal-salinity seawater during deposition time (Paleocene–Eocene) in the studied samples of the black shale from the Palana Formation.

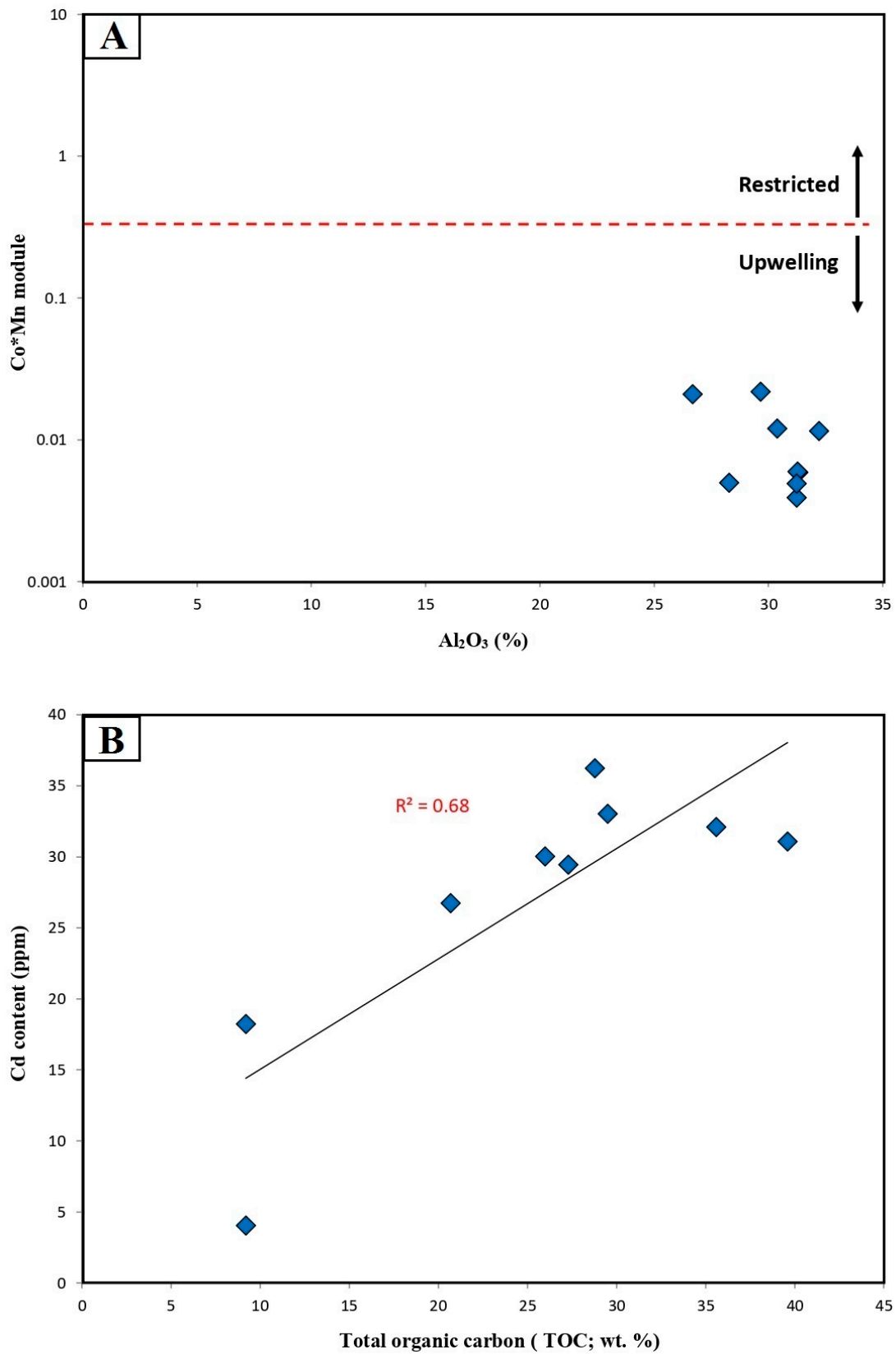


Figure 15. (A) Cross-plot of the Co × Mn vs. Al₂O₃ (after Sweere et al., [77]), showing upwelling activity during deposition time (Paleocene–Eocene) of the studied samples of black shale from the Palana Formation. (B) Relationship between TOC and Cd contents, showing a positive correlation.

5.2. Paleoclimate Evolution during the Paleocene–Eocene

Paleoclimatic conditions have been suggested as one of the major factors controlling the biological productivity within the photic zone of water columns, whereby the increased bioproductivity in the water is related to enhanced humid–warm climate conditions [15,16,82].

In this study, the paleoclimate reconstruction during the Paleocene–Eocene was attempted based on a variety of climate indexes, including Sr/Cu, Rb/Sr, Ga/Rb, and SiO₂/Al₂O₃ ratios. These ratios are proposed and widely used to reconstruct paleoclimate conditions [15,16,82].

The Sr/Cu ratio is extensively used to differentiate between a hot–arid (Sr/Cu > 10) and a warm–humid (1.3–5.0) climate [83,84]. In our case, the results show that the Sr/Cu ratios for most of the studied Palana shales exhibit low Sr/Cu ratios of <5 (0.76–1.35), suggesting that a warm and humid climate prevailed during the deposition of the Palana black shale facies. This interpretation of warm–humid climatic conditions is also consistent with the lower Rb/Sr values of less than 0.01, because high Rb/Sr ratios of >1 generally indicate cold and arid climates [85].

This finding of warm–humid climatic conditions is clearly supported by the cross-plot of Rb/Sr against Sr/Cu (Figure 16A).

Moreover, the major oxide-based observations, which involve SiO₂, Al₂O₃, K₂O, and Na₂O (Table 2), can also be used to characterize warm and humid climates [15,86]. The Al₂O₃ and K₂O major oxides and their associated trace elements gallium (Ga) and rubidium (Rb) can be used to examine the paleoclimatic conditions during the depositional period of the Palana organic-rich shale sediments [15]. The Ga is associated with Al₂O₃, whereas the Rb is associated with K₂O [87–89].

However, Al₂O₃ is generally enriched with kaolinite clay minerals and is known to be associated with warm climates [87,88], while K₂O is associated with illite clay minerals and reflects dry and cold climatic conditions [89].

In this study, the studied black shale of the Palana Formation is enriched in Al₂O₃ compared to very low K₂O, with a high ratio of Al/K (Table 2). The high abundance of Al₂O₃ is probably attributed to a kaolinite content of up to 27.3%, as clearly shown from the XRD and SPI-QEMSCAN results (Table 1; Figure 7). The presence of abundant kaolinite within the studied samples is believed to confirm the warm and humid climates during the Paleocene–Eocene, as supported by the Ga/Rb versus K₂O/Al₂O₃ binary diagram (Figure 16B) reported by Roy and Roser [90].

Moreover, the chemical weathering of the parent rock in the source area is generally affected by the climatic conditions [86]. It can be estimated using mineralogy and several geochemical indices of the major earth elements [91,92]. The chemical weathering intensity for sedimentary clastic rocks in the source area was also widely evaluated using the mineralogical compositions together with several weathering indexes, including the chemical index of alteration (CIA) and plagioclase index of alteration (PIA). These CIA and PIA weathering indexes were calculated based on Al₂O₃, CaO, Na₂O, and K₂O, as proposed by previous published works [91,93], and used by recent workers such as Armstrong-Altrin et al. [92] (2018) and He et al. [94]. These authors reported that the CIA and PIA, with a value of <60, indicate low weathering, 60–75 indicate moderate weathering, and values of >75 indicate intensive weathering. Accordingly, the studied shale samples show high values of the CIA and PIA indexes between 93.45 and 96.00 (Table 2), indicating a highly intensive degree of chemical weathering. This interpretation of the high chemical weathering trends is confirmed by the ternary diagram (A-CN-K) of Nesbitt and Young [95], as shown in Figure 17. Based on the A-CN-K ternary diagram, most of the studied shale samples of the Palana Formation plotted above the line of plagioclase and K-feldspar and clustered near the A-CN line towards the kaolinite composition, exhibiting a high degree of chemical weathering (Figure 17). This is in agreement with the high abundance of clay minerals, with high contributions of kaolinite and dickite (Table 1) that were derived from the weathering of silicates (primarily feldspar) [96]. Therefore, the original shale rocks

of the Palana Formation were highly weathered in warm and humid climates during the Paleocene–Eocene.

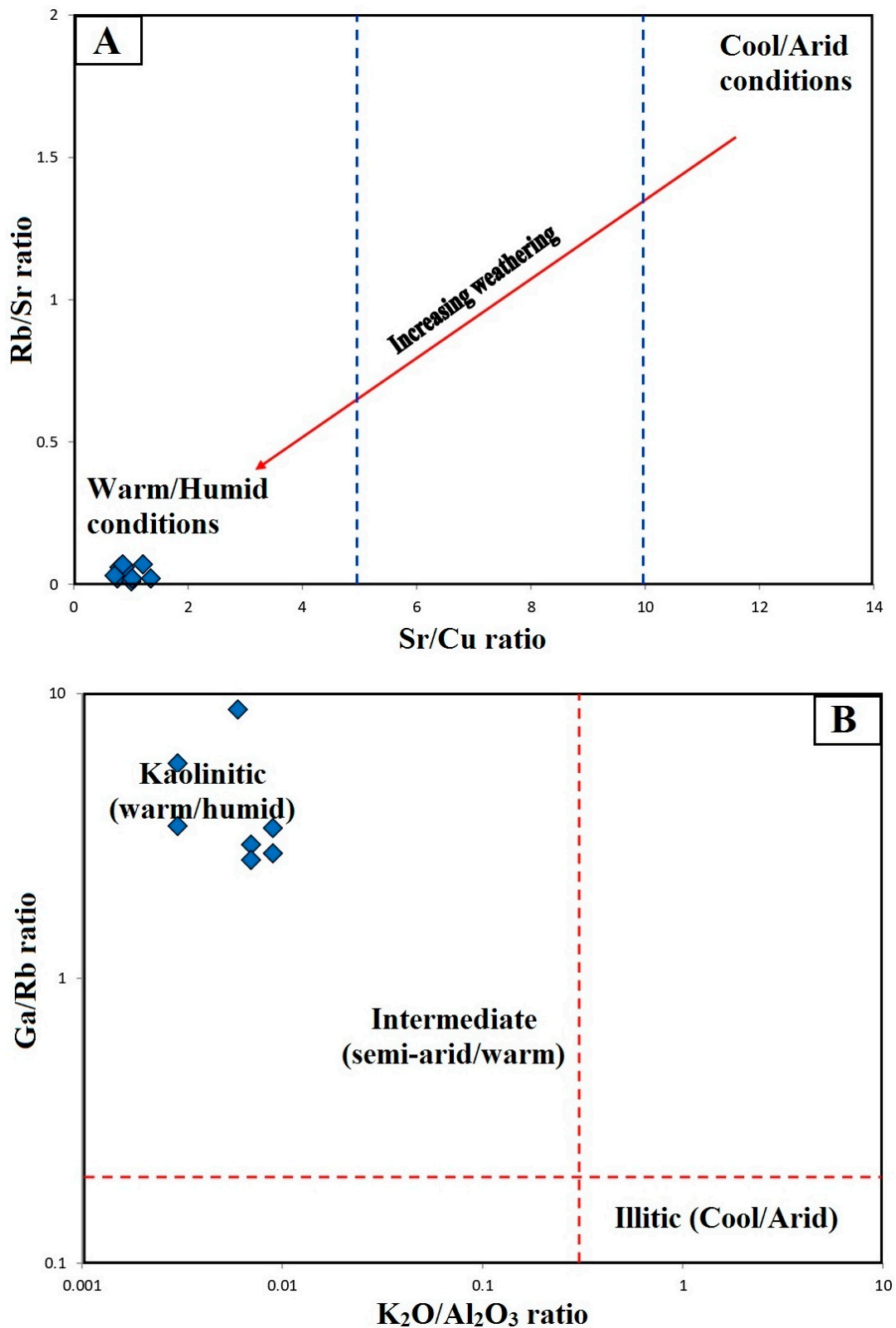


Figure 16. Diagrams related to warm and humid climatic conditions during deposition time (Paleocene–Eocene) of the studied samples of black shale from the Palana Formation. (A) Rb/Sr vs. Sr/Cu ratios plot and (B) Gr/Rb vs. K₂O/Al₂O₃ (after Roy and Roser [90]).

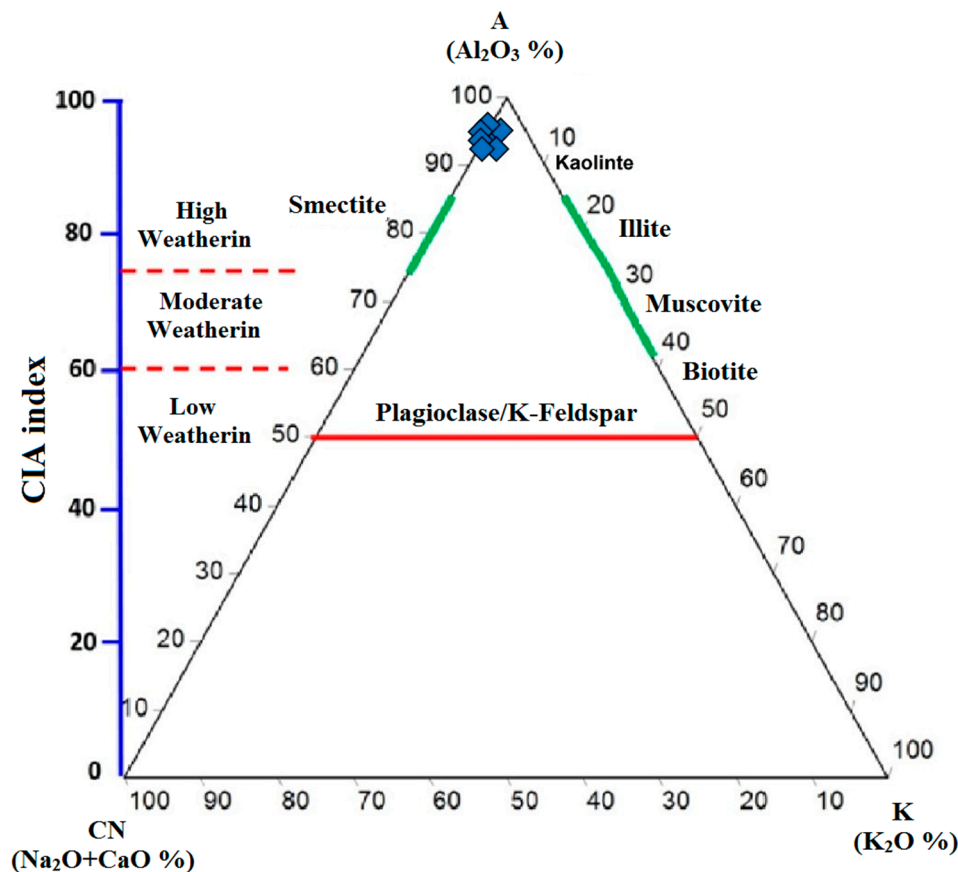


Figure 17. A-K-CN ternary diagram (after Nesbitt and Young [95]), showing a highly intensive degree of chemical weathering during deposition time (Paleocene–Eocene) in the studied samples of black shale from the Palana Formation.

In addition, the warm water period during the deposition of the Palana shale samples (Paleocene–Eocene) is also confirmed by the high abundance of phytoplankton blooms (Figure 5), since the growth and decomposition of phytoplankton are accelerated in warm water and decreased during cold-water conditions. In this way, the presence of high phytoplankton algae and other microorganisms in the analyzed Palana black shale sediments is probably due to the prevailing long warm-water episodes during the Paleocene–Eocene. However, the evidence for the presence of the richness of phytoplankton algae during the warm and humid climatic conditions is also demonstrated and supported by the occurrence of barite associated with organic matter (Figure 8B) and the relatively high barium (Ba) content in the black shale intervals of the Palana Formation (Table 2), which are tightly connected with a high primary phytoplankton productivity [97–99], because the upwelling brings abundant nutrients to the surface seawater during the same time (Figure 15A).

However, the nannofossil taxa, i.e., *Zeugrhabdotus erectus*, is considered a shelf species, and it was used as an indicator of high fertility [71–73]. Accordingly, the availability of *Zeugrhabdotus erectus* in the Palana shale samples (Figure 9A) is indicated by the high nutrient level on the sea surface during the precipitation of Palana shale sediments on the shelf. This high level of nutrients is associated with acceleration in hydrologic cycles and the weathering rate of preexisting rocks that has been promoted by warming on the sea surface [100,101].

5.3. Hydrothermal and Volcanic Activity during the Paleocene–Eocene

In order to estimate the hydrothermal activities during the Paleocene–Eocene, this study used hydrothermal geochemical indicators and a discrimination diagram of major and trace elements. The Fe and Mn elements can be employed to ascertain the influence of

hydrothermal activity on sedimentary rocks, which are mostly easily and actively enriched in sediments during hydrothermal activities [102]. The Fe and Mn were integrated together with Ti and used to calculate the $(\text{Fe} + \text{Mn})/\text{Ti}$ ratio, which is a good indicator to evaluate hydrothermal activities and their impact on the sedimentary rocks [102,103]. A $(\text{Fe} + \text{Mn})/\text{Ti}$ ratio of <15 provides a strong hydrothermal indication, while a $(\text{Fe} + \text{Mn})/\text{Ti}$ ratio of >15 indicates the influence of week-long hydrothermal activities during deposition under oxic conditions [60,104]. In this case, the studied black shale samples from the Palana Formation exhibit $(\text{Fe} + \text{Mn})/\text{Ti}$ ratios between 8.61 and 22.87, with an average value of 14.75 (Table 2), indicating generally strong hydrothermal activities during the Paleocene–Eocene. This result is confirmed by the relationship between the Fe and Mn elements and the sum of the Cu, Co, and Ni trace elements [104]. The richness of the Fe compared to Mn, Cu, Co, and Ni in all examined samples (Table 2) supports the inference of strong hydrothermal activities during the Paleocene–Eocene, which is quite similar to the Red Sea hydrothermal sedimentary signature based on the Fe–Mn– $(\text{Cu} + \text{Co} + \text{Ni}) \times 10$ ternary diagram of Qi et al. [104], as shown in Figure 18.

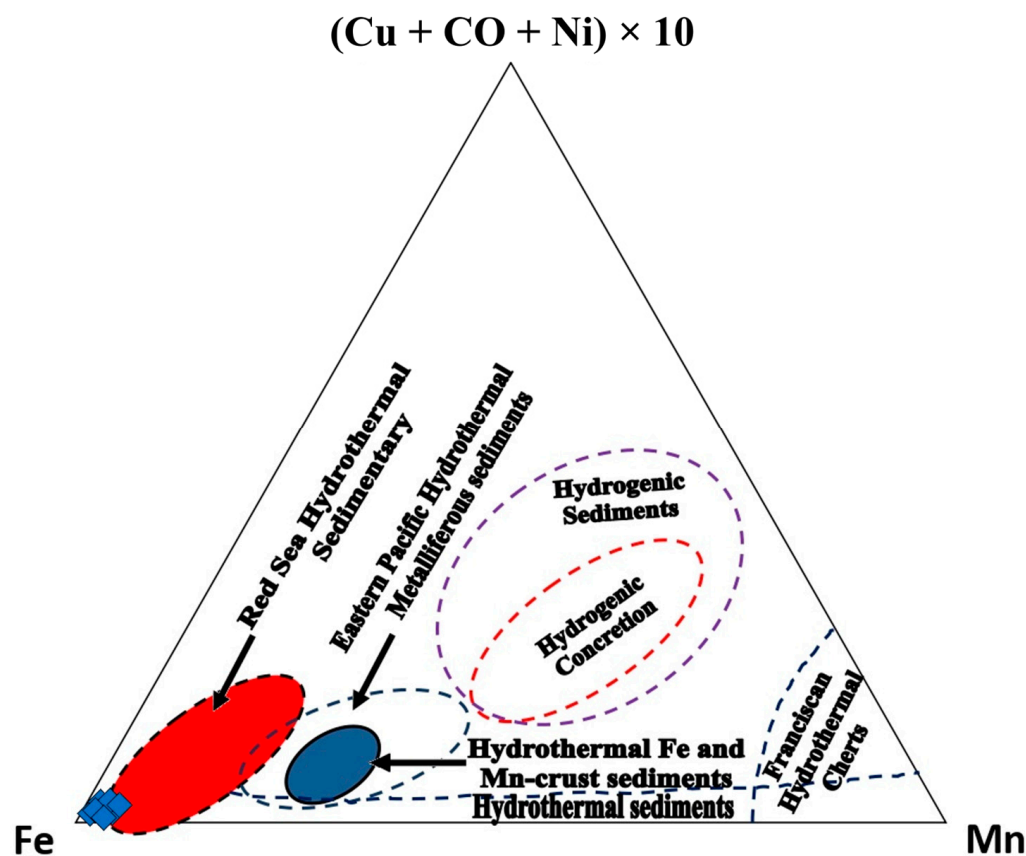


Figure 18. Fe–Mn– $(\text{Cu} + \text{Co} + \text{Ni}) \times 10$ ternary DIAGRAM (after Qi et al. [104]), showing high hydrothermal activity during deposition (Paleocene–Eocene) in the studied samples of black shale from the Palana Formation.

Moreover, the significant amounts of silica minerals (i.e., apophyllite and tridymite) together with zeolites in the studied black shale intervals (Table 1) are mostly considered to be of volcanic origin and support hydrothermal activities during the Paleocene–Eocene. Further, the hydrothermal activities during the deposition of the Palana shale sediments are also confirmed by the low concentrations of olivine minerals, which react with hydrothermal and weathering processes. Although the olivine is an unstable mineral and rapidly reacts by hydrothermal and weathering, the preservation of the olivine in the Palana shale sediments (Table 1) under humid and tropical conditions with hydrothermal activity during deposition may be attributed to the presence of the Fe-rich olivine, as demonstrated

by the high Fe content with a very low Mg content and the good correlation between the Fe content and olivine (Figure 10B). The Fe-rich olivine (fayalite) is considered to be more stable than the Mg-rich olivine (forsterite) [105], which could be brought both by river flows from the continent during the weathering of the volcanic rocks. The Fe-rich olivine (fayalite) varieties are found in intermediate and acidic igneous rocks [106]. This is consistent with the intermediate igneous rock origin for the Palana shale sediments, as demonstrated by a high abundance of SiO_2 content [92], with values of more than 40% (Table 2). The association between the Ti and Zr oxides also alludes to the intermediate igneous rock (Figure 19).

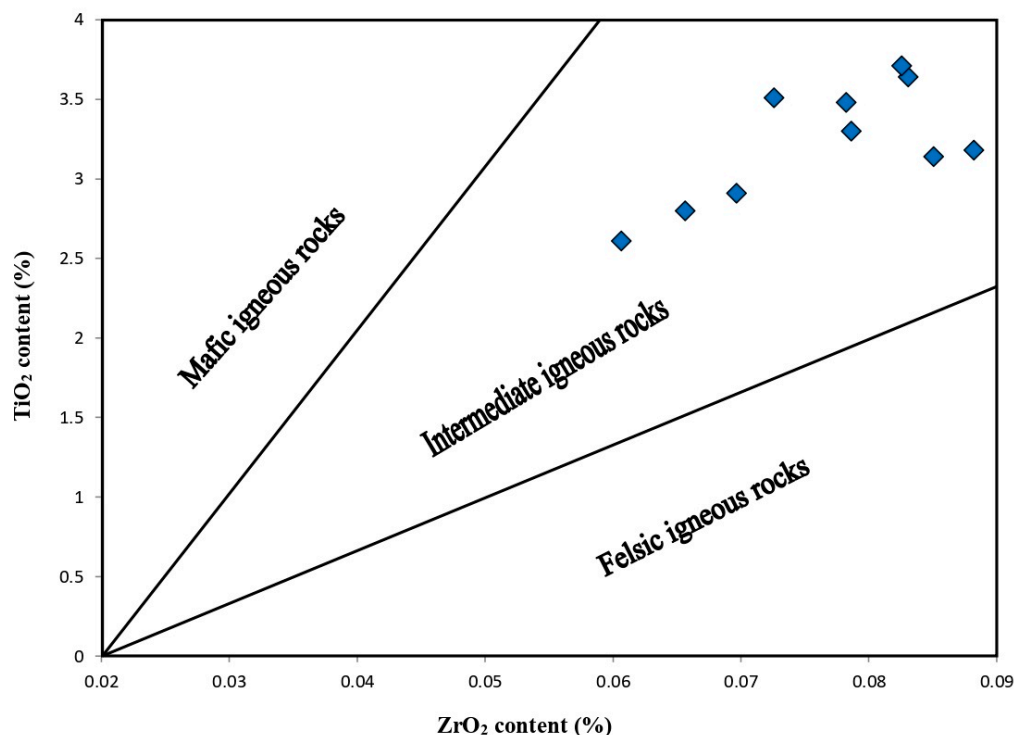


Figure 19. Plot of zircon against titanium oxides (after Hayashi et al. [107]) showing the intermediate igneous rock origin for the Palana shale sediments.

In addition, hydrothermal activity is commonly closely associated with the intrusion or eruption of volcanic rocks and related to a strong tectonic event.

In India, the volcanic eruption is a result of younger tectonic episodes related to the collision between the India and Asian plates during the Paleocene–Middle Eocene [30,31]. These volcanic activities provided an influx of large masses of ash accumulations in the Palana shale facies, as indicated by the relatively high contents of zeolites (up to 6.1%). However, when large amounts of volcanic ash are introduced into aqueous environments, it may lead to the dissolution of absorbed elements, including metal salts, thus mainly supplying a high concentration of nutrients for organisms and enhancing and increasing the primary bioproductivity [108,109]. In this case, nutrients such as phosphorus (P) are enriched in the studied Palana shale samples, with a P_2O_3 range of 0.14%–0.50% together with high Fe contents (Table 2), indicating that nutrients were transported and concentrated in these shales after deposition and hydrolyzation of volcanic ash [110]. This interpretation is confirmed by the significant positive correlation between P_2O_3 and zeolite derived from volcanic material (Figure 20), where the primary productivity of the aquatic organisms was due to the input of volcanic ash containing abundant nutrients and salts [110].

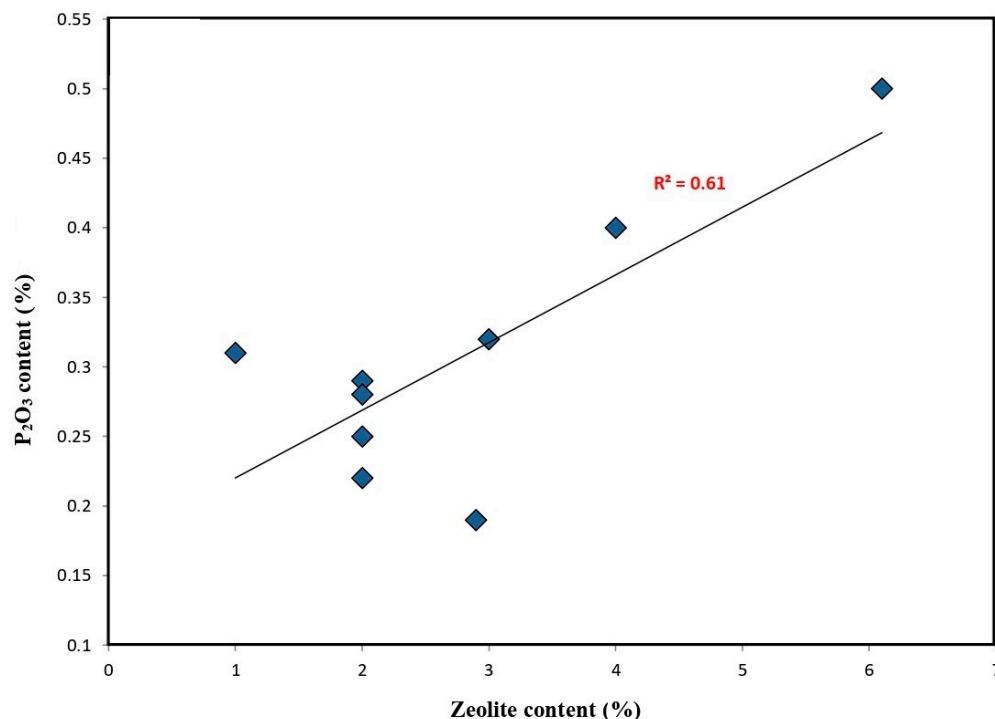


Figure 20. Plot of P₂O₅ content versus zeolite content of the studied black shale samples from the Palana Formation showing good positive correlations, with $R^2 = 0.61$.

6. Conclusions

Organic-rich shale facies of the Palana Formation from a Gurha mine in western Rajasthan, India, were investigated based on organic geochemistry, mineralogical, and elemental composition, together with microscopic examinations to evaluate the main sedimentary and paleoenvironmental factors and volcanic activity during the Paleocene–Eocene that influenced the high organic carbon accumulation. Based on the results, the following points are concluded:

- The black shale facies of the Paleocene–Eocene Palana Formation exhibit high TOC and S contents of up to 36.23 wt.% and 2.24 wt.%, respectively, revealing normal marine settings and anoxic environmental conditions.
- The Palana shales are clay-rich lithofacies, ranging from siliceous mudstone to silica-rich argillaceous mudstone, with a high abundance of clay and silica minerals, as indicated by XRD data together with species identification (SPI) and SEM of the QEMSCAN results.
- Microscopic examinations reveal that the OM in the Palana clay-rich facies was primarily derived from algae and other bacterial organisms, along with foraminifer assemblages, which favored marine anoxic environmental conditions.
- Different redox-sensitive trace elements along with their ratios in the clay-rich shale facies of the Palana Formation indicate anoxic environmental conditions were recognized during the Paleocene–Eocene period.
- The mineralogical and elemental compositions show a warm and humid climate, with an intensive degree of chemical weathering that took place during the deposition of the Paleocene–Eocene Palana clay-rich facies.
- The results highlighted in this study suggest that the high organic carbon accumulation in the black shale facies of the Palana Formation was mainly controlled by sedimentary factors, i.e., high bioproductivity and preservation of organic matter together with volcanic activities during the Paleocene–Eocene.

Author Contributions: Conceptualization, M.H.H., A.K. and A.K.S.; methodology, A.M.A. and K.A.M.; software, M.H.H., A.K. and A.R.; validation, A.R., W.N. and M.A. (Mohammed Almobarky); formal analysis, A.M.A. and K.A.M.; investigation, M.H.H., A.K., A.L., M.A. (Mohammed Almobarky) and W.N.; resources, A.K.S.; data curation, A.K. and A.K.S.; writing—original draft preparation, M.H.H., M.A. (Mohammad Alqudah) and A.L.; writing—review and editing, M.H.H., A.K., A.L. and A.R.; visualization, M.H.H., M.A. (Mohammad Alqudah) and A.L.; project administration, M.H.H., A.K. and A.K.S.; funding acquisition, M.H.H., A.K., A.K.S. and A.L. All authors have read and agreed to the published version of the manuscript.

Funding: The second author acknowledges the University of Malaya postdoctoral fellowship scheme associated with grant number IF064-2019. The authors extend their sincere appreciation to the Researchers Supporting Project number (RSP2024R92) at King Saud University in Riyadh, Saudi Arabia. This work was also supported by the Ministry of Science and Higher Education of the Russian Federation under the agreement number 075-15-2022-299.

Data Availability Statement: The datasets used and/or analysed during the current study available from the corresponding author on reasonable request due to the large storage nature of the dataset.

Acknowledgments: The authors extend their gratitude to the Director of RGIPT and Geology & Geochemistry laboratory at RGIPT for their assistance in the procuring the shale samples and for generously providing the essential facilities required for this study that were available. German Bayona and anonymous reviewers are thanked for the constructive comments that improved the original manuscript.

Conflicts of Interest: The authors declare no conflicts of interest since the research was conducted in the absence of any commercial or financial relationships that could be construed as a potential conflict of interest.

References

1. Jarvie, D.M.; Hill, R.J.; Ruble, T.E.; Pollastro, R.M. Unconventional shale-gas systems: The Mississippian Barnett Shale of north-central Texas as one model for thermogenic shale-gas assessment. *AAPG Bull.* **2007**, *91*, 475–499. [\[CrossRef\]](#)
2. Sohail, G.M.; Radwan, A.E.; Mahmoud, M. A review of Pakistani shales for shale gas exploration and comparison to North American shale plays. *Energy Rep.* **2022**, *8*, 6423–6442. [\[CrossRef\]](#)
3. Mukherjee, M.; Misra, S. A review of experimental research on Enhanced Coal Bed Methane (ECBM) recovery via CO₂ sequestration. *Earth-Sci. Rev.* **2018**, *179*, 392–410. [\[CrossRef\]](#)
4. Hakimi, M.H.; Wan Hasiah, A. Organic geochemical characteristics and oil generating potential of the Upper Jurassic Safer shale sediments in the Marib-Shabowah Basin, western Yemen. *Org. Geochem.* **2013**, *54*, 115–124. [\[CrossRef\]](#)
5. Ahmed, A.; Jahandad, S.; Hakimi, M.H.; Gharib, A.F.; Mehmood, S.; Kahal, A.Y.; Lashin, A. Organic matter characteristics and conventional oil potentials of shales from the Early Jurassic Datta Formation in the Upper Indus Basin, Northern Pakistan. *J. Asian Earth Sci.* **2022**, *224*, 104975. [\[CrossRef\]](#)
6. Li, T.Y.; He, S.; Yang, Z. The marine source rock formation conditions and control factors. *Geol. Sci. Technol. Inf.* **2008**, *27*, 63–70, (In Chinese with English abstract).
7. Zonneveld, K.A.F.; Versteegh, G.J.M.; Kasten, S.; Eglinton, T.I.; Emeis, K.-C.; Huguet, C.; Koch, B.P.; de Lange, G.J.; de Leeuw, J.W.; Middelburg, J.J.; et al. Selective preservation of organic matter in marine environments; processes and impact on the sedimentary record. *Biogeosciences* **2010**, *7*, 483–511. [\[CrossRef\]](#)
8. Bechtel, A.; Jia, J.L.; Strobl, S.A.I.; Sachsenhofer, R.F.; Liu, Z.J.; Gratzer, R.; Püttmann, W. Paleoenvironmental conditions during deposition of the Upper Cretaceous oil shale sequences in the Songliao Basin (NE China): Implications from geochemical analyses. *Org. Geochem.* **2012**, *46*, 76–95. [\[CrossRef\]](#)
9. Shu, T.; Dazhen, T.; Hao, X.; Jianlong, L.; Xuefeng, S. Organic geochemistry and elements distribution in Dahuangshan oil shale, southern Junggar Basin: Origin of organic matter and depositional environment. *Int. J. Coal Geol.* **2013**, *115*, 41–51.
10. Calvert, S.E.; Pedersen, T.F. Chapter fourteen elemental proxies for palaeoclimatic and palaeoceanographic variability in marine sediments: Interpretation and application. *Dev. Mar. Geol.* **2007**, *1*, 567–644.
11. Bordenave, M.L.; Espitalié, J.; Leplat, P.O.J.L.; Oudin, J.L.; Vandenbroucke, M. Screening techniques for source rock evaluation. In *Applied Petroleum Geochemistry*; Editions Technip: Paris, France, 1993; pp. 217–278.
12. Schwarzkopf, T.A. Model for prediction of organic carbon in possible source rocks. *Maine Pet. Geol.* **1993**, *10*, 478–492. [\[CrossRef\]](#)
13. Carroll, A.R.; Bohacs, K.M. Stratigraphic classification of ancient lakes: Balancing tectonic and climatic controls. *Geology* **1999**, *27*, 99–102. [\[CrossRef\]](#)
14. Katz, B.J. Controlling factors on source rock development—a review of productivity, preservation and sedimentation rate. In *The Deposition of Organic-Carbon-Rich Sediments: Models, Mechanisms, and Consequences*; Harris, N.B., Ed.; SEPM Special Publication: Claremore, OK, USA, 2005; Volume 82, pp. 7–16.

15. Hakimi, M.H.; Abdullah, W.H.; Alqudah, M.; Makeen, Y.M.; Mustapha, K.A. Reducing marine and warm climate conditions during the Late Cretaceous, and their influence on organic matter enrichment in the oil shale deposits of North Jordan. *Int. J. Coal Geol.* **2016**, *165*, 173–189. [[CrossRef](#)]
16. Jia, J.; Bechtel, A.; Liu, Z.; Susanne, A.I.; Strobl, P.S.; Reinhard, F.S. Oil shale formation in the upper cretaceous Nenjiang formation of the songliao basin (NE China): Implications from organic and inorganic geochemical analyses. *Int. J. Coal Geol.* **2013**, *113*, 11–26. [[CrossRef](#)]
17. Singh, A.K.; Hakimi, M.H.; Kumar, A.; Ahmed, A.; Abidin, N.S.Z.; Kinawy, M.; Mahdy, O.E.; Lashin, A. Geochemical and organic petrographic characteristics of high bituminous shales from Gurha mine in Rajasthan, NW India. *Sci. Rep.* **2020**, *10*, 22108. [[CrossRef](#)]
18. Kumar, A.; Hakimi, M.H.; Singh, A.K.; Abdullah, W.H.; Zainal Abidin, N.S.; Rahim, A.; Mustapha, K.A.; Yelwa, N.A. Geochemical and Petrological Characterization of the Early Eocene Carbonaceous Shales: Implications for Oil and Gas Exploration in the Barmer Basin, Northwest India. *ACS Omega* **2022**, *7*, 42960–42974. [[CrossRef](#)]
19. Kumar, V.; Chandra, R. Geology and evolution of Nagaur–Ganganagar basin with special reference to salt and potash mineralization. *Geol. Surv. India* **2005**, *62*, 151.
20. Singh, P.K.; Rajak, P.K.; Singh, V.K.; Singh, M.P.; Naik, A.S.; Raju, S.V. Studies on thermal maturity and hydrocarbon potential of lignites of Bikaner–Nagaur basin, Rajasthan. *Energy Explor. Exploit.* **2016**, *34*, 140–157. [[CrossRef](#)]
21. Singh, A.; Shivanna, M.; Mathews, R.P.; Singh, B.D.; Singh, H.; Singh, V.P.; Dutta, S. Paleoenvironment of Eocene lignite bearing succession from Bikaner–Nagaur Basin, western India: Organic petrography, palynology, palynofacies and geochemistry. *Int. J. Coal Geol.* **2017**, *181*, 87–102. [[CrossRef](#)]
22. Kumar, A.; Singh, A.K.; Paul, D.; Kumar, A. Evaluation of hydrocarbon potential with insight into climate and environment present during deposition of the Sonari lignite, Barmer Basin Rajasthan. *Energy Clim. Chang.* **2020**, *1*, 100006. [[CrossRef](#)]
23. Mathews, R.P.; Singh, B.D.; Singh, V.P.; Singh, A.; Singh, H.; Shivanna, M.; Chetia, R. Organo-petrographic and geochemical characteristics of Gurha lignite deposits, Rajasthan, India: Insights into the palaeovegetation, palaeoenvironment and hydrocarbon source rock potential. *Geosci. Front.* **2020**, *11*, 965–988. [[CrossRef](#)]
24. Roy, A.B.; Jakhar, S.R. *Geology of Rajasthan (Northwest India) Precambrian to Recent*; Scientific Publishers: Singapore, 2002.
25. Bhowmick, P.K. *Phanerozoic Petroliferous Basin of India*; Glimpses of Geoscience Research in India: New Delhi, India, 2008; pp. 253–268.
26. Pollastro, R.M. Ghaba Salt Basin province and Fahud Salt Basin province—Oman: Geological overview and total petroleum systems. *United States Geol. Surv. Bull.* **1999**, *2167*, 1–41.
27. Al-Husseini, M.I. Origin of the Arabian plate structures: Amar collision and Najd Rift. *GeoArabia* **2000**, *5*, 527–542. [[CrossRef](#)]
28. Dmitry, A.; Al-Husseini, M.I.; Yumiko, I. Review of middle east Paleozoic plate tectonics. *GeoArabia* **2007**, *12*, 5–56.
29. Shukla, A.; Jasper, A.; Uhl, D.; Mathews, R.P.; Singh, V.P.; Chandra, K.; Chetia, R.; Shukla, S.; Mehrotra, R.C. Paleo-wildfire signatures revealing co-occurrence of angiosperm-gymnosperm in the early Paleogene: Evidences from woody charcoal and biomarker analysis from the Gurha lignite mine, Rajasthan, India. *Int. J. Coal Geol.* **2023**, *265*, 104164. [[CrossRef](#)]
30. Zhu, B.; Kid, W.S.F.; Rowley, D.B.; Currie, B.S.; Shafique, N. Age of Initiation of the India–Asia Collision in the East-Central Himalaya. *J. Geol.* **2005**, *113*, 265–285. [[CrossRef](#)]
31. Acharyya, S.K. Evolution of the Himalayan Paleogene foreland basin, influence of its litho-packet on the formation of thrust related domes and windows in the Eastern Himalayas—A review. *J. Asian Earth Sci.* **2007**, *31*, 1–17. [[CrossRef](#)]
32. Aitchison, J.C.; Ali, J.R.; Davis, A.M. When and where did India and Asia collide. *J. Geophys. Res.* **2007**, *112*, B05423. [[CrossRef](#)]
33. Acharya, S.K.; Saha, P. Age and Tectono-Magmatic Setting of Abor Volcanics, Siang Window, Eastern Himalays Syntaxial Area, India. Available online: https://www.researchgate.net/publication/264002018_Age_and_tectono-magmatic_setting_of_abor_volcanics_siang_window_eastern_himalayan_syntaxial_Area_India (accessed on 15 November 2023).
34. Shukla, A.; Mehrotra, R.C. Paleoequatorial rain forest of western India during the EECO: Evidence from *Uvaria* L. fossil and its geological distribution pattern. *Hist. Biol.* **2014**, *26*, 693–698. [[CrossRef](#)]
35. Shukla, A.; Mehrotra, R.C. Early Eocene (~50 My) legume fruits from Rajasthan. *Curr. Sci.* **2016**, *11*, 465–467.
36. Shukla, A.; Mehrotra, R.C. Early Eocene plant megafossil assemblage of western India: Paleoclimatic and paleobiogeographic implications. *Rev. Palaeobot. Palynol.* **2018**, *258*, 123–132. [[CrossRef](#)]
37. Schopf, J.M. *Field Description and Sampling of Coal Beds*; US Government Printing Office: Washington, DC, USA, 1960; p. 67.
38. Taylor, G.; Teichmüller, M.; Davis, A.; Diessel, C. *Organic Petrology*; Gebrüder Borntraeger: Stuttgart, Germany, 1998.
39. Qian, G.; Li, Y.; Gerson, A.R. Applications of surface analytical techniques in Earth Sciences. *Surf. Sci. Rep.* **2015**, *70*, 86–133. [[CrossRef](#)]
40. Amao, A.O.; Al-Otaibi, B.; Al-Ramadan, K. High-resolution X-ray diffraction datasets: Carbonates. *Data Brief* **2022**, *42*, 108204. [[CrossRef](#)] [[PubMed](#)]
41. Ayling, B.; Rose, P.; Petty, S.; Zemach, E.; Drakos, P. QEMSCAN® (Quantitative Evaluation of Minerals by Scanning Electron Microscopy): Capability and application to fracture characterization in geothermal systems. In Proceedings of the Thirty-Seventh Workshop on Geothermal Reservoir Engineering, Stanford, CA, USA, 30 January–1 February 2012.
42. Alqubalee, A.M.; Babalola, L.O.; Abdullatif, O.M.; Eltom, H.A. Geochemical Characterization of Subsurface Upper Ordovician Glaciogenic Deposits: Implications for Provenance, Tectonic Setting, and Depositional Environments. *Arab. J. Sci. Eng.* **2021**, *47*, 7273–7291. [[CrossRef](#)]

43. Berner, R.A.; Raiswell, R. Burial of organic carbon and pyrite sulfur in sediments over Phanerozoic time: A new theory. *Geochim. Cosmochim. Acta* **1983**, *47*, 855–862. [[CrossRef](#)]
44. Hedges, J.I.; Keil, R.G. Sedimentary organic matter preservation: An assessment and speculative synthesis. *Mar. Chem.* **1995**, *49*, 81–115. [[CrossRef](#)]
45. Dowey, P.J.; Taylor, K.G. Diagenetic mineral development within the Upper Jurassic Haynesville-Bossier Shale, UAS. *Sedimentology* **2020**, *67*, 47–77. [[CrossRef](#)]
46. Forjanés, P.; Astilleros, J.M.; Fernández-Díaz, L. The Formation of Barite and Celestite through the Replacement of Gypsum. *Minerals* **2020**, *10*, 189. [[CrossRef](#)]
47. Martínez-Ruiz, F.; Paytan, A.; González-Munoz, M.T.; Jroundi, F.M.M.; Abad, M.M.; Lam, P.J.; Horner, T.J.; Kastner, M. Barite Precipitation on Suspended Organic Matter in the Mesopelagic Zone. *Front. Earth Sci.* **2020**, *8*, 567714. [[CrossRef](#)]
48. Algeo, T.J.; Maynard, J.B. Trace-element behavior and redox facies in core shales of Upper Pennsylvanian Kansas-type cyclothems. *Chem. Geol.* **2004**, *206*, 289–318. [[CrossRef](#)]
49. Barwise, A.J.G. Role of nickel and vanadium in petroleum classification. *Energy Fuels* **1990**, *4*, 647–652. [[CrossRef](#)]
50. Wei, S.; Hu, M.; He, S.; Yang, W.; He, Q.; Cai, Q.; Li, P. Sedimentary Environment Interpretation and Organic Matter Enrichment of the Lower Cambrian Shuijingtuo Shale in the Yichang Slope, South China: Insight from Sedimentary Geochemical Proxies with Major/Trace Elements. *J. Mar. Sci. Eng.* **2023**, *11*, 2018. [[CrossRef](#)]
51. Tribouillard, N.; Algeo, T.J.; Lyons, T.; Riboulleau, A. Trace metals as paleoredox and paleoproductivity proxies: An update. *Chem. Geol.* **2006**, *232*, 12–32. [[CrossRef](#)]
52. Bechtel, A.; Gratzner, R.; Sachsenhofer, R.F. Chemical characteristics of upper cretaceous (Turonian) jet of the gosau group of gams/hieflau (styria, Austria). *Int. J. Coal Geol.* **2001**, *46*, 27–49. [[CrossRef](#)]
53. Galarraga, F.; Reategui, K.; Martínez, A.; Martínez, M.; Llamas, J.F.; Marquez, G. V/Ni ratio as a parameter in palaeoenvironmental characterisation of nonmature medium-crude oils from several Latin American basins. *J. Pet. Sci. Eng.* **2008**, *61*, 9–14. [[CrossRef](#)]
54. Hatch, J.R.; Leventhal, J.S. Relationship between inferred redox potential of the depositional environment and geochemistry of the upper pennsylvanian (missourian) Stark shale member of the dennis limestone, wabaunsee county, Kansas, USA. *Chem. Geol.* **1992**, *99*, 65–82. [[CrossRef](#)]
55. Jones, B.; Manning, D.A. Comparison of geochemical indices used for the interpretation of palaeoredox conditions in ancient mudstones. *Chem. Geol.* **1994**, *111*, 111–129. [[CrossRef](#)]
56. Algeo, T.J.; Liu, J.S. A re-assessment of elemental proxies for paleoredox analysis. *Chem. Geol.* **2020**, *540*, 119549. [[CrossRef](#)]
57. Arthur, M.A.; Sageman, B.B. Marine black shales: A review of depositional mechanisms and significance of ancient deposits. *Annu. Rev. Earth Planet Sci.* **1994**, *22*, 499–551. [[CrossRef](#)]
58. Large, D.J.; Gize, A.P. Pristane/phytane ratios in the mineralized Kupferschiefer of the Fore-Sudetic Monocline, southwest Poland. *Ore Geol. Rev.* **1996**, *11*, 89–103. [[CrossRef](#)]
59. Xu, J.; Liu, Z.; Bechtel, A.; Meng, Q.; Sun, P.; Jia, J.; Cheng, L.; Song, Y. Basin evolution and oil shale deposition during Upper cretaceous in the songliao basin (NE China): Implications from sequence stratigraphy and geochemistry. *Int. J. Coal Geol.* **2015**, *149*, 9–23. [[CrossRef](#)]
60. Wang, Z.; Fu, X.; Feng, X.; Song, C.; Wang, D.; Chen, W.; Zeng, S. Geochemical features of the black shales from the Wuyu Basin, southern Tibet: Implications for paleoenvironment and paleoclimate. *Geol. J.* **2017**, *52*, 282297. [[CrossRef](#)]
61. Orhan, H.; Delikan, A.; Demir, A.; Kapan, S.; Olgun, K.; Ozmen, A.; Sayin, Ü.; Ekici, G.; Aydin, H.; Nazik, A. Geochemical evidences of paleoenvironmental changes in late quaternary lacustrine sediments of the konya closed basin (konya, Turkey). In *Patterns and Mechanisms of Climate, Paleoclimate and Paleoenvironmental Changes from Low Latitude Regions*; Zhang, Z., Khelifi, N., Mezghani, A., Heggy, E., Eds.; Springer: Berlin, Germany, 2019; pp. 73–76.
62. Remírez, M.N.; Algeo, T.J. Paleosalinity determination in ancient epicontinental seas: A case study of the T-OAE in the Cleveland Basin (UK). *Earth Sci. Rev.* **2020**, *201*, 103072. [[CrossRef](#)]
63. Read, J.F.; Kerans, C.; Weber, L.J.; Sarg, H.F.; Wright, F.M. Milankovitch sea-level changes, cycles and reservoirs on carbonate platforms in green-house and ice-house worlds. *SEPM Short Course* **1995**, *35*, 1–81.
64. Price, G.D. The evidence and implications of polar-ice during the Mesozoic. *Earth Sci. Rev.* **1999**, *48*, 183–210. [[CrossRef](#)]
65. Vincent, B.; Rambeau, C.; Emmanuel, L.; Loreaue, J.P. Sedimentology and trace element geochemistry of shallow-marine carbonates: An approach to paleoenvironmental analysis along the Pagny-sur-Meuse section (Upper Jurassic, France). *Facies* **2006**, *52*, 69–84. [[CrossRef](#)]
66. Omar, N.; McCann, T.; Al-Juboury, A.I.; Franz, S.O. Petrography and geochemistry of the Middle-Upper Jurassic Banik section, northernmost Iraq—Implications for paleoredox, evaporitic and diagenetic conditions. *N. Jb. Geol. Paleont. Abh.* **2020**, *297*, 125–152. [[CrossRef](#)]
67. Dashtgard, S.E.; Wang, A.; Pospelova, V.; Wang, P.-L.; La Croix, A.; Ayranci, K. Salinity indicators in sediment through the fluvial-to-marine transition (Fraser River, Canada). *Sci. Rep.* **2022**, *12*, 14303. [[CrossRef](#)]
68. Deng, H.W.; Qian, K. *Analysis on Sedimentary Geochemistry and Environment*; Science Technology Press: Lanzhou, China, 1993; pp. 15–85. (In Chinese)
69. Lei, B.; Que, H.P.; Hu, N.; Niu, Z.J.; Wang, H. Geochemistry and sedimentary environments of the Palaeozoic siliceous rocks in western Hubei. *Sediment. Geol. Tethyan Geol.* **2002**, *22*, 70–79. (In Chinese with English Abstract)

70. Zhang, K.; Liu, R.; Liu, Z.J.; Li, L.; Wu, X.P.; Zhao, K.A. Influence of palaeoclimate and hydrothermal activity on organic matter accumulation in lacustrine black shales from the lower cretaceous Bayingebi Formation of the Yin'e Basin, China. *Palaeogeogr. Palaeoclimatol. Palaeoecol.* **2020**, *560*, 110007.
71. Herrle, J.O.; Pross, J.; Friedrich, O.; Koeßler, P.; Hemleben, C. Forcing mechanisms for mid-Cretaceous black shale formation: Evidence from the Upper Aptian and Lower Albian of the Vocontian Basin (SE France). *Palaeogeogr. Palaeoclimatol. Palaeoecol.* **2003**, *190*, 399–426. [[CrossRef](#)]
72. Bornemann, A.; Pross, J.; Reichelt, K.; Herrle, J.O.; Hemleben, C.; Mutterlose, J. Reconstruction of short-term palaeoceanographic changes during the formation of the Late Albian 'Niveau Breistroffer' black shales (Oceanic Anoxic Event 1d, SE France). *J. Geol. Soc.* **2005**, *162*, 623–639. [[CrossRef](#)]
73. Bottini, C.; Mutterlose, J. Integrated stratigraphy of Early Aptian black shales in the Boreal Realm: Calcareous nannofossil and stable isotope evidence for global and regional processes. *Newsl. Stratigr.* **2012**, *45*, 115–137. [[CrossRef](#)]
74. Strakhov, N.M. *Fundamentals of the Theory of Lithogenesis*; Publishing House of the Academy of Sciences of the USSR: Moscow, Russia, 1960.
75. Sajid, Z.; Ismail, M.S.; Zakariah, M.; Tsegab, H.; Gámez Vintaned, J.A.; Hanif, T.; Ahmed, N. Impact of Paleosalinity, Paleoredox, Paleoproductivity/Preservation on the Organic Matter Enrichment in Black Shales from Triassic Turbidites of Semanggol Basin, Peninsular Malaysia. *Minerals* **2020**, *10*, 915. [[CrossRef](#)]
76. Brumsack, H.J. The trace metal content of recent organic carbon-rich sediments: Implications for Cretaceous black shale formation. *Palaeogeogr. Palaeoclimatol. Palaeoecol.* **2006**, *232*, 344–361. [[CrossRef](#)]
77. Sweere, T.; van den Boorn, S.; Dickson, A.J.; Reichart, G.-J. Definition of new trace-metal proxies for the controls on organic matter enrichment in marine sediments based on Mn, Co, Mo and Cd concentrations. *Chem. Geol.* **2006**, *441*, 235–245. [[CrossRef](#)]
78. Zhang, B.; Yao, S.; Wignall, P.B.; Hu, W.; Ding, H.; Liu, B.; Ren, Y. Widespread coastal upwelling along the eastern paleo-tethys margin (south China) during the middle Permian (Guadalupian): Implications for organic matter accumulation. *Mar. Petrol. Geol.* **2018**, *97*, 113–126. [[CrossRef](#)]
79. Lu, Y.; Jiang, S.; Lu, Y.; Xu, S.; Shu, Y.; Wang, Y. Productivity or preservation? The factors controlling the organic matter accumulation in the late Katian through Hirnantian Wufeng organic-rich shale, South China. *Mar. Petrol. Geol.* **2019**, *109*, 22–35. [[CrossRef](#)]
80. Lyons, T.W.; Werne, J.P.; Hollander, D.J.; Murray, R.W. Contrasting sulfur geochemistry and Fe/Al and Mo/Al ratios across the last oxic-to-anoxic transition in the Cariaco Basin, Venezuela. *Chem. Geol.* **2003**, *195*, 131–157. [[CrossRef](#)]
81. Conway, T.M.; John, S.G. Biogeochemical cycling of cadmium isotopes along a high-resolution section through the North Atlantic Ocean. *Geochim. Cosmochim. Acta* **2015**, *148*, 269283. [[CrossRef](#)]
82. Adegoke, A.K.; Abdullah, W.H.; Hakimi, M.H.; Sarki Yandoka, B.M. Geochemical characterisation of Fika Formation in the Chad (Bornu) Basin, northeastern Nigeria: Implications for depositional environment and tectonic setting. *Appl. Geochem.* **2014**, *43*, 1–12. [[CrossRef](#)]
83. Song, Y.; Liu, Z.; Meng, Q.; Xu, J.; Sun, P.; Cheng, L.; Zheng, G. Multiple controlling factors of the enrichment of organic matter in the upper cretaceous oil shale sequences of the Songliao basin, NE China: Implications from geochemical analyses. *Oil Shale* **2016**, *33*, 142–166. [[CrossRef](#)]
84. Xu, C.; Shan, X.L.; He, W.T. The fluctuation of warm paleoclimatic controls on lacustrine carbonate deposition in the Late Cretaceous (late Santonian), Southern Songliao Basin, Northeast China. *Int. J. Earth Sci.* **2021**, *111*, 85–102. [[CrossRef](#)]
85. Bai, Y.Y.; Liu, Z.J.; Sun, P.C.; Liu, R.; Hu, X.F.; Zhao, H.Q.; Xu, Y.B. Rare earth and major element geochemistry of Eocene fine-grained sediments in oil shale and coal-bearing layers of the Meihe Basin, Northeast China. *J. Asian Earth Sci.* **2015**, *97*, 89–101. [[CrossRef](#)]
86. Moradi, A.V.; Sarı, A.; Akkaya, P. Geochemistry of the Miocene oil shale (hançili formation) in the Çankırı-Çorum basin, Central Turkey: Implications for paleoclimate conditions, source–area weathering, provenance and tectonic setting. *Sediment. Geol.* **2016**, *341*, 289–303. [[CrossRef](#)]
87. Hieronymus, B.; Kotschoubey, B.; Boulegue, J. Gallium behavior in some contrasting lateritic profiles from Cameroon and Brazil. *J. Geochem. Explor.* **2001**, *72*, 147–163. [[CrossRef](#)]
88. Beckmann, B.; Floegel, S.; Hofmann, P.; Schulz, M.; Wagner, T. Orbital forcing of Cretaceous river discharge in tropical Africa and ocean response. *Nature* **2005**, *437*, 241–244. [[CrossRef](#)]
89. Ratcliffe, K.T.; Wright, A.M.; Hallsworth, C.; Morton, A.; Zaitlin, B.A.; Potocki, D.; Wray, D.S. Alternative correlation techniques in the petroleum industry: An example from the (lower cretaceous) basal quartz, southern Alberta. *Bull. Am. Assoc. Pet. Geol.* **2004**, *88*, 419–432.
90. Roy, D.K.; Roser, B.P. Climatic control on the composition of Carboniferous-Permian Gondwana sediments, Khalaspir basin, Bangladesh. *Gondwana Res.* **2013**, *23*, 1163–1171. [[CrossRef](#)]
91. Nesbitt, H.W.; Young, G.M. Early Proterozoic climates and plate motions inferred from major element chemistry of lutites. *Nature* **1982**, *299*, 715–717. [[CrossRef](#)]
92. Armstrong-Altrin, J.S.; Ramos-Vázquez, M.A.; Hermenegildo-Ruiz, N.Y.; Madhavaraju, J. Microtexture and U–Pb geochronology of detrital zircon grains in the Chachalacas beach, Veracruz State, Gulf of Mexico. *Geol. J.* **2020**, *56*, 2418–2438. [[CrossRef](#)]
93. Fedo, C.M.; Nesbitt, H.W.; Young, G.M. Unraveling the effects of potassium metasomatism in sedimentary rocks and paleosols, with implications for paleoweathering conditions and provenance. *Geology* **1995**, *23*, 921–924. [[CrossRef](#)]

94. He, T.H.; Lu, S.F.; Li, W.H.; Sun, D.Q.; Pan, W.Q.; Zhang, B.S.; Tan, Z.Z.; Ying, J.F. Paleoweathering, hydrothermal activity and organic matter enrichment during the formation of earliest Cambrian black strata in the Northwest Tarim Basin, China. *J. Pet. Sci. Eng.* **2020**, *189*, 106987. [[CrossRef](#)]
95. Nesbitt, H.W.; Young, G.M. Prediction of some weathering trends of plutonic and volcanic-rocks based on thermodynamic and kinetic considerations. *Geochim. Cosmochim. Acta* **1984**, *48*, 523–1534. [[CrossRef](#)]
96. Deer, W.A.; Howie, R.A.; Zussman, J. *An Introduction to Rock-Forming Minerals*; Longman Group Ltd.: London, UK, 1975; p. 528.
97. Ran, B.; Liu, S.; Jansa, L.; Sun, W.; Yang, D.; Ye, Y.; Wang, S.; Luo, C.; Zhang, X.; Zhang, C. Origin of the Upper Ordovician–lower Silurian cherts of the Yangtze block, South China, and their palaeogeographic significance. *J. Asian Earth Sci.* **2015**, *108*, 1–17. [[CrossRef](#)]
98. Wang, Y.; Chen, B.; Li, X.; Wang, H.; Chang, L.; Jiang, S. Sedimentary characteristics of up-welling facies shale in lower Silurian Longmaxi Formation, northeast sichuan area. *Acta Pet. Sin.* **2018**, *39*, 1092–1102.
99. Zou, C.; Zhu, R.; Chen, Z.Q.; Ogg, J.G.; Wu, S.; Dong, D.; Qiu, Z.; Wang, Y.; Wang, L.; Lin, S.; et al. Organic-matter-rich shales of China. *Earth Sci. Rev.* **2019**, *189*, 51–78. [[CrossRef](#)]
100. Tejada, M.L.G.; Suzuki, K.; Kuroda, J.; Coccioni, R.; Mahoney, J.J.; Ohkouchi, N.; Sakamoto, T.; Tatsumi, Y. Ontong Java Plateau eruption as a trigger for the Early Aptian oceanic anoxic event. *Geology* **2009**, *37*, 855–858. [[CrossRef](#)]
101. Blättler, C.L.; Jenkyns, H.C.; Reynard, L.M.; Handerson, G.M. Significant increases in global weathering during Oceanic Anoxic Events 1a and 2 indicated by calcium isotopes. *Earth Planet. Sci. Lett.* **2011**, *309*, 77–88. [[CrossRef](#)]
102. Adachi, M.; Yamamoto, K.; Sugisaki, R. Hydrothermal chert and associated siliceous rocks from the northern Pacific their geological significance as indication of ocean ridge activity. *Sediment. Geol.* **1986**, *47*, 125–148. [[CrossRef](#)]
103. Skinner, B. The many origins of hydrothermal mineral deposits. In *Geochemistry of Hydrothermal Ore Deposits*, 2nd ed.; Barnes, H.L., Ed.; John Wiley & Sons: New York, NY, USA, 1979; pp. 3–21.
104. Qi, H.W.; Hu, R.Z.; Su, W.C.; Qi, L.; Feng, J.Y. Continental hydrothermal sedimentary siliceous rock and genesis of superlarge germanium (Ge) deposit hosted in coal: A study from the Lincang Ge deposit, Yunnan, China. *Sci. China Ser. D Earth Sci.* **2004**, *47*, 973–984. [[CrossRef](#)]
105. Howie, R.A.; Zussman, J.; Deer, W. *An Introduction to the Rock-Forming Minerals*; Longman, P., Ed.; Mineralogical Society of Great Britain and Ireland: Middlesex, UK, 1992; p. 696.
106. Huang, P.M.; Wang, M.K. Minerals, Primary. In *Encyclopedia of Soils in the Environment*; Goss, M.J., Oliver, M.A., Eds.; Academic Press: Cambridge, MA, USA, 2005; pp. 500–510.
107. Hayashi, K.I.; Fujisawa, H.; Holland, H.D.; Ohmoto, H. Geochemistry of ~1.9 Ga sedimentary rocks from northeastern labrador. *Can. Geochim. Cosmochim. Acta* **1997**, *61*, 4115–4137. [[CrossRef](#)] [[PubMed](#)]
108. Langmann, B.; Zaksek, K.; Hort, M.; Dfituutt Iuggen, S. Volcanic ash as fertilizer for the surface ocean. *Atmos. Chem. Phys.* **2010**, *10*, 38913899. [[CrossRef](#)]
109. Duggen, S.; Olgun, N.; Croot, P.; Hoffmann, L.; Dietze, H.; Delmelle, P.; Teschner, C. The role of airborne volcanic ash for the surface ocean biogeochemical iron-cycle: A review. *Biogeosciences* **2010**, *7*, 827–844. [[CrossRef](#)]
110. Chen, X.; Zhang, B.; Huang, H.; Mao, Z. Controls on Organic Matter Accumulation of the Triassic Yanchang Formation Lacustrine Shales in the Ordos Basin, North China. *ACS Omega* **2021**, *6*, 26048–26064. [[CrossRef](#)]

Disclaimer/Publisher’s Note: The statements, opinions and data contained in all publications are solely those of the individual author(s) and contributor(s) and not of MDPI and/or the editor(s). MDPI and/or the editor(s) disclaim responsibility for any injury to people or property resulting from any ideas, methods, instructions or products referred to in the content.